Bai *et al. Cell & Bioscience* (2025) 15:59
https://doi.org/10.1186/s13578-025-01399-6

Cell & Bioscience

RESEARCH Open Access

Disrupting lipid homeostasis with CAV2 in OSCC triggers apoptosis, lipolysis, and mitochondrial dysfunction by transcriptional repression of PPARγ

Yuting Bai[1], Mingjing Jiang[1], Xiaojie Chen[1,2*] and Gang Zhou[1,2*]

Abstract

Background Abnormal lipid droplet (LD) dynamics in oral squamous cell carcinoma (OSCC) indicate lipid metabolism alterations that facilitate malignancy progression. However, the specific mechanisms by which disruptions in lipid homeostasis affect malignancy processes remain poorly understood. This study investigated the role of LD-associated protein Caveolin2 (CAV2) in OSCC lipid homeostasis and progression.

Methods The clinical relevance of *CAV2* in OSCC was assessed through transcriptomics, single-cell sequencing, and functional validation in OSCC cells. *CAV2* knockdown via shRNA was used to analyze its effects on growth, apoptosis, lipid homeostasis, and mitochondrial function. RNA sequencing, lipidomics, and molecular docking elucidated mechanisms of lipid metabolic disruption. Lipolysis was evaluated via glycerol release, lipidomics, and expression of related genes and proteins. Seahorse assays were used to evaluate mitochondrial dysfunction by analyzing mitochondrial respiration, while additional experiments assessed ROS levels, MMP, morphology, mass, and organelle interactions. In vivo, studies examined tumor progression in nude mice implanted with *CAV2*-knockdown OSCC cells. The regulatory role of PPARγ on CAV2 was explored through bioinformatics, correlation analysis, and dual-luciferase assays. Coimmunoprecipitation assessed CAV2 and NCOR1 binding with PPARγ, while the PPARγ inverse agonist T0070907 was used to enhance NCOR1-mediated repression of CAV2.

Results *CAV2* was upregulated in OSCC and correlated with poor clinical outcomes. *CAV2* knockdown increased apoptosis, reduced proliferation, and disrupted lipid homeostasis, elevating polyunsaturated fatty acids (PUFAs). Regulatory networks responsible for PUFA accumulation were mapped in *CAV2*-knockdown OSCC cells, from upstream regulators to downstream effects. Furthermore, lipolysis and mitochondrial dysfunction were also enhanced following *CAV2* silencing. In vivo, *CAV2* knockdown suppressed OSCC progression. Mechanistically, PPARγ regulated CAV2 transcription via NCOR1, but OSCC cells disrupted this repression. The PPARγ inverse agonist T0070907 restored

*Correspondence:
Xiaojie Chen
chenxiaojie-whu@whu.edu.cn
Gang Zhou
zhougang@whu.edu.cn

Full list of author information is available at the end of the article

NCOR1-mediated repression, synergistically enhancing the effects of *CAV2* knockdown on apoptosis, lipolysis, and mitochondrial dysfunction.

Conclusions Alteration of CAV2 disrupted lipid homeostasis and inhibited OSCC progression by affecting key processes, including apoptosis, lipolysis, and mitochondrial dysfunction. The disruption was driven by the dysregulation of the PPARγ/NCOR1 axis, highlighting the potential of targeting CAV2 and its interaction with PPARγ as a therapeutic strategy for OSCC.

Graphical Abstract

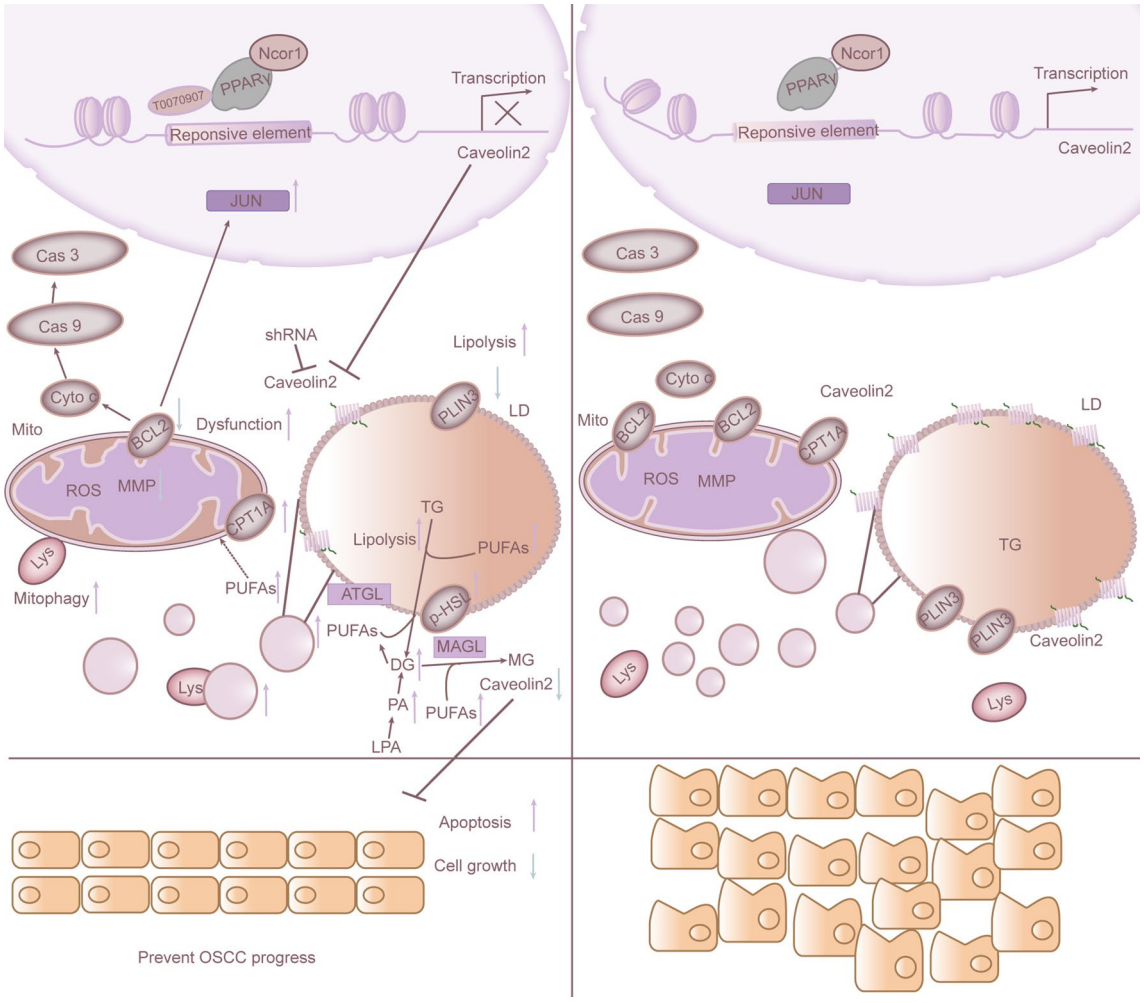

Highlights

- CAV2 regulated the lipid droplet dynamics, and when *CAV2* was silenced, it enhanced lipolysis and resulted in the deposition of polyunsaturated fatty acids, which might flow to mitochondria in OSCC.
- Suppression of *CAV2* induced apoptosis and compromised mitochondrial function.
- PPARγ failed to recruit NCOR1 as a transcriptional repressor to reduce CAV2 in OSCC.
- The PPARγ inverse agonist T0070907 enhanced CAV2 deletion and promoted apoptosis, lipolysis, and mitochondrion dysfunction when elevating the recruiting of NCOR1.

Keywords Caveolin2, Lipid droplet, Polyunsaturated fatty acids, Mitochondrial dysfunction, Oral squamous cell carcinoma, Peroxisome proliferator-activated receptor γ, Integrated lipidomic and transcriptomic analyses, Molecular docking

Introduction

Head and neck cancer ranks as the seventh most prevalent disease globally, with 890,000 new cases and 450,000 deaths recorded annually [1]. Oral squamous cell carcinoma (OSCC) is the predominant malignancy affecting the head and neck area [1, 2]. Individuals with OSCC are often diagnosed with advanced localized illnesses and have a combination therapy consisting of surgery, radiation, and chemotherapy. Nevertheless, patients with severe or recurrent OSCC do not have a substantial improvement in survival [3]. Acquiring a comprehensive understanding of the mechanisms that cause the malignant progression of OSCC and identifying new therapeutic targets and medications is of utmost importance.

The progression of cancer is closely linked to alterations in lipid metabolism. The interaction between these crucial mechanisms in cancer is not yet understood. Lipid droplets (LDs) comprise a phospholipid monolayer enclosing a core of neutral lipids, which is essential in controlling lipid metabolism within cells [4]. The disruption of LD-mediated lipid metabolism in OSCC has lately attracted attention. Our earlier study has discovered that LDs accumulate even in the early precancerous stage of OSCC [5, 6]. LD-associated proteins, located on the exterior layer of LDs, are vital for preserving LD integrity, regulating lipid accumulation, lipolysis, and lipid utilization, and facilitating interactions with cellular processes such as signaling and lipid distribution [4].

Caveolin2 (CAV2) is a critical component of the caveolae structure within cell membranes and is also located in the outermost layer of phospholipids in LDs [7], where it participates in signal transduction [8] and serves as a hub for lipid transport [9]. CAV2 is involved in cellular growth and survival [10], and its knockout in mice leads to mitochondrial aggregation, indicating a close relationship between CAV2 and mitochondria [11]. Furthermore, we and others have demonstrated that CAV2 contributes to the advancement of cancers [6, 12–14]. For instance, the CAV2 protein facilitates kidney cancer growth by activating the PI3K signaling pathway [14]. However, the mechanisms of CAV2-induced alternations of lipid metabolism in cancers, including OSCC, remain unclear.

The most extensively researched LD-associated proteins are the five members of the perilipin (PLIN) family [15]. Deletion of PLIN2 and PLIN3 facilitated lipolysis via autophagy [16]. PLIN2 influences HSL/ATGL-mediated lipolysis. Two routes manage lipolysis. Initially, cytosolic lipases and triglycerides in cells are degraded into fatty acids (FAs) and glycerol by enzymes ATGL, HSL, and MAGL, enabling their release for energy production or other metabolic activities. Furthermore, macrolipophagy refers to the process in which autophagosomes engulf LDs and transport them to lysosomes. Once within the lysosome, lipases inside break down the LDs through hydrolysis [17]. Our previous work has identified that CAV2 is positively associated with PLIN3 during different histopathological stages of OSCC [6]. Nevertheless, the role of CAV2 in regulating lipolysis has not been explored.

Peroxisome proliferator-activated receptor γ (PPARγ) is a nucleus receptor that binds to eicosanoids and regulates lipid metabolism, cell apoptosis, and the formation of new mitochondria [18]. PPARγ can also modulate the expression of lipolysis-related genes, promoting the activation of the lipolytic pathway [19]. PPARγ influences mitochondrial-mediated cellular metabolism, producing ROS and electron flow, which supports the apoptosis processes [20]. Patients with OSCC showing high levels of PPARγ expression generally have a poorer prognosis than those with lower PPARγ expression [21], which suggests that, in addition to ligand activation, the elevated levels of the PPARγ receptor may contribute to the unfavorable prognosis. Furthermore, nuclear receptors can switch between transcriptional repression and activation depending on the presence of ligands and coactivators or corepressors. However, regulation of transcription by PPARγ through the recruitment of transcriptional repressors for tumor suppression remains unexplored in OSCC. Nuclear receptor corepressor 1 (NCOR1) is essential in regulating PPARγ. In the absence of ligands, NCOR1 interacts with PPARγ, suppressing the expression of target genes [22]. Dysregulation of the PPARγ/NCOR1 pathway leads to lipid metabolism alternation, cellular proliferation, and epigenetic modifications, resulting in cancer [23, 24]. Despite substantial research on the ligand-dependent mechanisms of PPARγ, the role of NOCoR1 as a corepressor remains insufficiently explored. Thus, understanding the interaction between PPARγ and NCOR1 and its impact on CAV2 regulation may reveal the broader regulatory functions of PPARγ and offer new therapeutic insights for OSCC. Based on these findings, we hypothesize that knocking down *CAV2* may enhance apoptosis. lipolysis, and mitochondrial dysfunction while inhibiting OSCC progression. Additionally, it is essential to explore whether PPARγ influences CAV2-mediated lipid reprogramming in OSCC.

This study analyzed the clinical significance and oncogenic potential of *CAV2* in OSCC patients. Cell growth and apoptosis were observed after interference with *CAV2*. The impact of CAV2 on the dynamics and functions of LDs in OSCC cells was explored. OSCC cells with *CAV2* silenced were selected for further study. Whole lipid changes and the mechanisms underlying *CAV2*-mediated disruption of lipid homeostasis were investigated by transcriptome and lipidomics. Utilizing lipidomics and RNAseq data, along with glycerol release assays and transmission electron microscopy (TEM) analyses to observe organelle alterations during lipolysis,

molecular changes were validated, confirming the occurrence of lipolysis. The effects of *CAV2* knockdown on mitochondrial function and structure were explored. *CAV2*-knockdown OSCC cells were subcutaneously implanted into nude mice to provide an in vivo model for observing the effects of *CAV2* inhibition. The transcriptional regulation of CAV2 by PPARγ was elucidated by bioinformatics prediction, dual luciferase report, and coimmunoprecipitation (Co-IP) assays. The transcriptional repression in conjunction with *CAV2* silencing treatment was evaluated on cell growth, apoptosis, lipolysis, and mitochondria dysfunction.

Materials and methods

Analyses of TCGA

RNAseq data from 330 OSCC patients and 32 normal samples were received via the TCGA website (http://cancergenome.nih.gov/), focusing on the mRNA level of *CAV2* and its association with clinical outcomes and other biomarkers. The RNAseq data underwent processing to derive Transcripts Per Million (TPM) values, which involved quality control procedures such as normalization utilizing R software (Ver. 4.2.1). The expression of *CAV2* and the calculation of *P* values for statistical significance were performed with the Stats (Ver. 4.2.1) and Car (Ver. 2.1-6) packages. Subsequently, the expression data of *CAV2* in TCGA datasets, along with the associated *P* values, were displayed with ggplot2 (Ver. 3.3.6). Survival analysis was performed with the Survminer (Ver. 0.4.9) and survival (Ver. 3.3.1) utilizing the Log-rank for evaluating survival based on *CAV2* expression levels, with Kaplan-Meier curves visualizing these differences. In addition, ggplot2 was employed to show the relationship between *CAV2* expression and clinical outcomes, including clinical T stage, histologic grade, clinical N stage, clinical M stage, age, and gender. The study used Pearson and Spearman correlation tests and *P*-values to identify relationships between *CAV2* and *PPARG* levels and several biomarkers. Specifically, for *CAV2*, the biomarkers included *PLIN3*, *PNPLA2*, *LIPE*, *BCL2*, *Caspase3 (CAS3)*, and *Caspase9 (CAS9)*; for *PPARG*, the biomarkers included *CAV2*, *PLIN3*, *LIPE*, *MGLL*, and *BCL2*.

Moreover, the study incorporated data from TISCH, which compiles scRNA sequence data from sources like Gene Expression Omnibus (GEO) and ArrayExpress [25]. Single-cell RNAseq data for OSCC were obtained from the TISCH database, explicitly utilizing the dataset HNSC_GSE103322. This dataset encompasses comprehensive single-cell transcriptomic information from HNSCC patients focusing on the oral cavity [26]. This work used TISCH to decipher *CAV2* and *PPARγ* expression in OSCC at the single-cell level.

Cell lines and culture

Human OSCC cell lines SCC25 and SCC9 cells were cultivated with Dulbecco's Modified Eagle Medium: Nutrient Mixture F-12 (DMEM: F12) (Gibco, Grand Island, NY, USA) supplemented with 10% fetal bovine serum (FBS, Biological Industries, Kibbutz Beit-Haemek, Israel) and 1% penicillin/streptomycin (P/S) solution (Gibco). Human embryonic kidney 293T cells and OSCC cell lines CAL27 and HSC2 cells were cultured with DMEM (Gibco) containing 10% FBS and 1% P/S solution. These cell lines were all acquired through the American Type Culture Collection (Manassas, VA, USA). Additionally, the OKF4 cell line, an immortalized human oral keratinocyte line provided by Dr. Zhou Gang from Wuhan University, China, was cultured in a specific keratinocyte serum-free medium (Gibco) added epidermal growth factors [27]. Cultivation conditions for all cells included a humid atmosphere maintained at 37 °C with 5% CO_2. The above cell lines were subjected to short tandem repeat profiling and verified to be devoid of mycoplasma infection. More details regarding these cell lines, including OKF4, SCC25, CAL27, SCC9, HSC2, and 293T, could be found in the supplementary files: Table S1.

Lentiviral transfection

Three types of recombinant lentiviruses were employed to manipulate the expression of the *CAV2* gene. Firstly, shCAV2-1 (KD) and shCAV2-2 (KD-2) lentiviruses were used to knock down the expression of CAV2, with shControl-1 (NC) and shControl-2 (NC-2), containing empty vectors, serving as negative controls. The detailed sequences of these shRNAs were provided in Supplementary files: Table S2. Secondly, to upregulate CAV2 expression, the CAV2OE recombinant lentivirus was utilized, with the control CAV2CON containing an empty vector. Lentivirus samples were obtained from GenePharma (Suzhou, China). After 6–8 h of lentivirus cultivation, the cells were chosen with 2 μg/mL puromycin.

Real-time quantitative PCR

The total RNA was extracted using TRIzol (AXYGEN, NY, USA), and the reverse transcription was conducted using the HiScript III RT SuperMix for qPCR Kit (Vazyme, Nanjing, China). The Real-time quantitative PCR (RT-qPCR) was performed using the ChamQ Universal SYBR qPCR Master Mix (Vazyme) on the CFX Connect™aReal-Time System (Bio-Rad Laboratories, Hercules, CA, USA). The gene alterations were determined using the comparative approach, namely the $2^{-\Delta\Delta Ct}$ method. The trials were conducted three times each. The primers were listed in Supplementary files: Table S3.

Western blot

The cell protein was extracted using a radioimmunoprecipitation technique. The protein concentration was determined using the bicinchoninic acid technique. The protein was isolated using sodium dodecyl sulfate-polyacrylamide gel electrophoresis (10%) and transferred to a 0.22-μm PVDF membrane (Millipore Sigma, Burlington, MA, USA). Before incubation with the primary antibodies, the membranes were treated with 3% bovine serum albumin (BSA) to prevent unwanted binding. The membranes were exposed to the appropriate secondary antibodies the next day. The ECL kit (Thermo Fisher Scientific in Massachusetts, USA) was used to visualize blots and quantify them using the NIH ImageJ software. The protein expression was evaluated by calculating the ratio between the signals from the protein of GAPDH. The antibodies utilized in this study were presented in Supplementary files: Table S4.

Cell proliferation assay

A total of 5,000 cells were seeded in each well of the 96-well plate and left to grow for specified durations to evaluate the effect on the growth of OSCC cells. Subsequently, a culture mix containing 10% Cell Counting Kit-8 (CCK-8, Dojindo Molecular Technologies, Kumamoto, Japan) solution was utilized to culture cells for 1 h. The amount of light absorbed at a wavelength of 450 nm was measured using a microplate reader (BioTek, located in Winooski, VT, USA). Cell proliferation was determined following the provided directions.

Colony formation assay

500 cells were distributed in each well of the six-well plate and left to incubate for 14 days. Subsequently, the colonies were treated with a 4% paraformaldehyde (PFA, Servicebio, Wuhan, China) solution and then stained using crystal violet (Servicebio). The plates were rinsed with phosphate-buffered saline (PBS, Gibco) and then air-dried for colony assessment using a digital camera.

EdU incorporation assay

The studies were conducted according to the previously provided description [28]. The detection of EdU was performed using the BeyoClick™ EdU Cell Proliferation Kit with Alexa Fluor 594 (Beyotime, Shanghai, China). In summary, OSCC cells were evenly distributed in culture plates and incubated with the EdU reagents. After two hours, the cells were treated with 4% PFA. Subsequently, cell staining was carried out according to the manufacturer's instructions. Five distinct fields were acquired using a microscope (BX53F, Olympus, Tokyo, Japan).

Flow cytometry

The experiments were conducted using the methods reported in a prior study [29]. Concisely, an annexin V-APC/propidium iodide (PI) apoptosis detection kit (KGA1030, Keygen Biotech, Nanjing, China) was used to identify apoptotic cells, following the instructions provided by the manufacturer. The cellular concentration was modified to 10^6 /ml. Subsequently, the cells underwent wash, followed by treatment with PI and Annexin V–APC for 15 min. The cells were then assessed using a CytoFLEX flow cytometry (Beckman Coulter, Pasadena, CA, USA).

RNAseq data analysis

Total RNA was purified from CAV2NC SCC25 and CAV2KD SCC25 cells using a phenol-chloroform method. A detailed methodology for total RNA extraction was provided in Supplementary Materials and Methods: S1.1. There were three biological replicates for the SCC25 cells. RNA was qualified and quantified using a NanoDrop and Agilent 2100 Bioanalyzer (Thermo Fisher Scientific), respectively. Detailed library construction methodology and quality filtering were provided in the Supplementary Materials and Methods: S1.2 and S1.3.

Then, the clean reads were mapped onto the reference genome using HISAT2 [30], followed by novel gene prediction, SNP & INDEL calling, and gene-splicing detection. Clean reads were mapped to reference using Bowtie2 v2.2.5 [31], and then gene expression levels were calculated with RSEM v1.2.12 [32]. The heatmap was drawn using pheatmap (v1.0.8) in R software. Essentially, differential expression analysis was performed using the DEseq2 (v1.4.5) [33] with Q value ≤ 0.05 and fold change (FC) > 0 or < 0. To take an insight into the change of phenotype, differentially expressed genes (DEGs) were subjected to GO (http://www.geneontology.org/) and KEGG (https://www.kegg.jp/) functional enrichment analysis using Phyper (https://en.wikipedia.org/wiki/Hypergeometric_distribution) based on Hypergeometric test [30]. The significant levels of terms and pathways were corrected by Q value with a rigorous threshold (Q value ≤ 0.05) by Bonferroni [34].

Immunofluorescence staining

This experiment was performed as previously described [35]. Cells were cultivated on confocal dishes for 24 h at 2×10^5 cells/mL density. For LD staining, cells were incubated at 37 °C in a serum-free medium containing 2 μg/mL BODIPY™ 493/503 solution diluted in DMSO for 30 min, followed by washing. Next, the cells were fixed with 4% PFA and permeabilized with 0.1% Triton X-100. Then, cells were blocked with 3% BSA solutions and exposed to primary antibodies. The following day, the cells underwent incubation with secondary antibodies.

Subsequently, cells were subjected to a 10-minute incubation period with DAPI (Beyotime). Finally, the cells were treated with an antifade mounting medium (Beyotime) to prevent fluorescence quenching. The antibody concentrations used were indicated in the Supplementary files: Table S4.

To observe the expression of CAV2 protein in SCC25 and CAL27 cells, cells were captured using a confocal microscope (FV1200, Olympus) and FV10-ASW Viewer software (Ver. 4.2b, Olympus). The 488 nm, 559 nm, and 405 nm wavelengths were employed to excite BODIPY™ 493/503, Dylight 594, and DAPI, respectively. To calculate the colocalization of CAV2 protein and LDs, super-resolution imaging was performed using an STED microscope (Abberior Instruments, Göttingen, Germany). Excitation lasers with wavelengths of 405 nm, 488 nm, and 561 nm were employed in combination with a 100 × 1.45 NA oil immersion objective (Olympus). Depletion was achieved using a single STED laser operating at 775 nm. Image deconvolution was performed using Huygens Professional software (Ver. 24.04, SVI, Netherlands) to enhance resolution and clarity.

The quantifications shown in Figure S4C and S4D were examined using the ImageJ software by generating and analyzing intensity projections. For colocalization analysis, regions of interest were manually selected to focus on LDs identified based on BODIPY staining. The Pearson correlation coefficient was calculated using the 'Coloc2' plugin in ImageJ to quantify the degree of colocalization between CAV2 protein marked by Dylight 594 and BODIPY-stained LDs, with colocalization scatterplots generated using the 'Colocalization Finder' plugin to visualize the overlap, where points closer to the diagonal indicate higher colocalization. Three separate experiments were conducted for each condition. For each experimental condition, seven fields of cells were captured.

Oil red O staining

The oil red O staining was conducted using the previously reported methodology [6]. In summary, the cells were grown and transferred to Petri dishes. Next, the cells were treated with 4% PFA to fix them, stained with oil red O solution, counterstained with hematoxylin, and sealed with glycerol gelatin. Seven fields were captured at a magnification of 400× using a microscope (BX53F). The LD numbers per cell, LD area per cell, or the average area of LDs, measured in pixels, were assessed using Image-pro Plus software (IPP, ver. 6.0, Media Cybernetics, Silver Springs, MD, USA). The tissue-frozen samples underwent staining using the identical procedure employed for cells.

Lipidomic analysis

The lipids from subconfluent CAV2NC SCC25 and CAV2KD SCC25 cells were extracted using the modified Folch method, as described in Supplementary Materials and Methods: S1.4. The entire description of the lipid separation and detection approach, including the equipment utilized, column material, ion modes, composition of mobile phases, and gradient elution parameters, could be found in Supplementary Materials and Methods S1.5. The specific MS1 and MS2 data acquisition parameters for this study were included in the Supplementary Materials and Methods: S1.6.

Raw MS data were analyzed using LipidSearch (Ver. 4.1, Thermo Fisher Scientific) for peak processing and identification [36]. Further analysis was conducted with the metaX R package (BGI, Shenzhen, China) [37]. First, the low-weight ions with relative standard deviation relative standard deviation (RSD) > 30% were filtered out to ensure the data quality. Data were then corrected by the QC-based robust LOESS signal correction (QC-RLSC) method [38]. The univariate analysis employed FC detection and t-tests for significance testing. For multivariate analysis, principal component analysis (PCA) and orthogonal partial least-squares discriminant analysis (OPLS-DA) were used to identify differential ions across clusters. Ions with a variable importance of projection (VIP) ≥ 1 were considered significant. Based on results from quality control (QC) sample detections, the RSD threshold was set below 30% for error reduction, reflected in the FC of lipids. Based on results from QC sample detections, the RSD threshold was set below 30% for error reduction, reflected in lipids' FC. The identification of lipids was further performed through the Human Metabolome Database, KEGG, and LipidMaps. Finally, metabolites meeting the criteria (VIP ≥ 1, $P < 0.05$, FC ≤ 0.83, or FC ≥ 1.2) were selected as significantly different. Based on the different lipids, KEGG analysis was performed using the R language, especially the " clusterProfiler " package [39]. Relevant statistical analysis of sublipids was performed using GraphPad Prism 8.0 (GraphPad Software, San Diego, California, USA).

Integrated lipidomic and transcriptomic analyses

Integrative analyses were performed to correlate lipidomic and transcriptomic data, focusing on lipids and genes involved in shared pathways. Differential genes and lipids were identified using regularised Canonical Correlation Analysis (rCCA) with criteria set at Q < 0.05 and FC < -1 or > 1 [40]. The mixOmics package [41] was utilized for this analysis, employing the block.splsda function to identify significant genes and lipids and visualize the results with plotVar and Circos plots. A correlation network was created by identifying significant couples with a correlation coefficient > 0.9 or < -0.9 and a *P*-value < 0.5

between the transcriptome and lipidomic. The top 20 high-correlation gene-lipid pairs were selected for a correlation chord diagram, illustrating the most robust associations [40]. Network extension and identification were performed using Cytoscape (Ver.3.9.1). Pathway comparisons between the two omics were conducted using Venn diagrams to identify shared and unique metabolic pathways. KEGG pathway enrichment analysis was performed to assess the degrees of enrichment of genes and lipids in each pathway. Pathway bubble charts were used to visualize the substantial enrichment of differentially expressed genes and lipids.

Molecular Docking

The N-terminal regulatory region of carnitine palmitoyltransferase 1 (CPT1A) in humans can be attributed to the fatty acids FA(20:4), FA(20:5), FA(22:5), and FA(24:6). The PubChem database (https://pubchem.ncbi.nlm.nih.gov/) was queried to retrieve the structures in the SDF format for the chemicals FA(20:4), FA(20:5), FA(22:5), and FA(24:6). The protein structures were obtained in the PDB format from the RCSB database (https://www.rcsb.org/). Subsequently, the MOE (Ver. 2015, Montreal, QC, Canada) software was employed to eliminate solvent molecules and ligands, introduce hydrogen, compute charges, and allocate atomic types. Finally, the ligand docking module was utilized to simulate and compute molecular docking. The unique conformations of the target ligand were chosen for the study of the binding mode using MOE.

The human PPARγ ligand binding domain of PPARγ was also traced back to the corresponding PPARγ inverse agonist T0070907 using the same method as described in the previous paragraph.

Lipolysis measurement

Glycerol release into the culture medium served as an indicator of lipolysis, as previously outlined [42]. OSCC cells were deprived of nutrients in media containing 2% FA-free BSA (Biosharp, Anhui, China) for 3 h before the experiment. The medium was replenished with the vehicle (DMSO) or isoproterenol (ISO, 100 nM). Following 1 h of incubation, 100 μL of culture media was transferred to a 96-well plate. Subsequently, glycerol release into the medium was quantified utilizing the Amplex Red Glycerol Assay Kit (Beyotime) according to the manufacturer's instructions. Plates were incubated at 37 °C for 1 h, and fluorescence intensity was detected with an excitation wavelength of 560 nm and an emission wavelength of 590 nm. The protein content was quantified utilizing the Pierce BCA reagent from Thermo Fisher Scientific. The glycerol concentration was adjusted based on the protein content of the cells within the same well. All studies were conducted using four biological replicates.

TEM

The cultured cells were immobilized using a 2.5% (w/v) glutaraldehyde solution in 0.1 M phosphate buffer with a pH of 7.4. The cells were fixed after the initial fixation using a cold solution of 1% (w/v) osmium tetroxide in water. The cells were immersed in 1% uranyl acetate for 2 h. Cells were then dehydrated in a series of ethanol washes of 50%, 75%, 80%, and 95% each for 15 min, 100% ethanol, and acetone for 15 min twice. The samples were treated with a mixture of acetone and EMbed-812 resin in a ratio of 2:1 for 1 h. Then, they were infiltrated with a mixture of acetone and EMbed-812 resin in a ratio of 1:1 for 24 h. Finally, the samples were treated with EMbed-812 resin twice for 2 h. The specimens were subsequently inserted into molds containing new resin and subjected to polymerization in an oven at 37 °C for 12 h, followed by an oven temperature of 60 °C for 2 days. The samples were obtained at around 70 nm and placed on Cu grids coated with formvar and carbon. They were then treated with 2% uranyl acetate in 50% acetone and stained with 0.2% lead citrate. The sections were examined using TEM at an acceleration voltage of 80 kilovolts (kV), and images were captured using a Gatan Orius 2k X 2k digital camera. TEM analysis was conducted on three separate samples, and cells were randomly selected for imaging and analysis. The frequency of LD-lysosome contacts was determined by dividing the number of cells having LD-lysosome interactions by the total number of cells counted. The quantity of interactions between mitochondria and lysosomes in each cell was quantified to analyze mitophagy.

Quantification of ROS, mitochondrial membrane potential, mitochondrial mass, and mitochondrial morphology

To detect changes in intracellular ROS, mitochondrial membrane potential (MMP), mitochondrial mass, and mitochondrial morphology, a DCFH-DA probe (Beyotime), JC-1 assay kit (Beyotime), and Mito-Tracker Red CMXRos (Beyotime) were used, following the manufacturer's instructions. According to the manufacturer's instructions, fluorescence was measured using a BX53F microscope. For detecting intracellular ROS, MMP, and mitochondrial mass, DCFH-DA (488 nm excitation), JC-1 (561 nm excitation for high membrane potential), MitoTracker Red CMXRos (561 nm excitation), and DAPI (405 nm excitation) were used.

The STED microscopy was employed for mitochondrial morphology analysis. The STED microscope was from Abberior Instruments. The DAPI signal was visualized using the 405 nm excitation channel, while Mito-Tracker Red CMXRos was observed using the 561 nm excitation channel. Image acquisition was performed using a 100 × 1.4 NA oil immersion objective (Olympus), with optical resolution adjusted to approximately 50 nm

to capture fine mitochondrial details. Data processing, including deconvolution, was conducted using Huygens Professional (Ver. 24.04) software.

Mitochondrial respiration

Mitochondrial respiration was assessed using the Seahorse XF Cell Mito Stress Test Kit and the Seahorse XFe-24 Analyzer (Seahorse Bioscience, North Billerica, MA, USA). 3×10^4 cells/well were seeded into XF Cell Culture Microplates (Agilent Technologies, Santa Clara, CA, USA). After incubation, cells were transferred to Seahorse XF assay medium supplemented with 10 mM glucose, 2 mM L-glutamine, and 1 mM sodium pyruvate and equilibrated for 1 h in a CO_2-free incubator. The assay involved sequential injections of 1.5 μM oligomycin to inhibit ATP synthase, 1.5 μM FCCP to uncouple oxidative phosphorylation and determine maximum respiratory capacity, and 0.5 μM rotenone with 0.5 μM antimycin A to inhibit complexes I and III for non-mitochondrial oxygen consumption. O_2 consumption rate (OCR) was measured in real-time after each injection, with data normalized to cell numbers and analyzed using the Seahorse XFe24/XF24 Analyzer, providing a detailed profile of non-mitochondrial oxygen consumption, basal respiration, maximum respiratory capacity, proton leak, ATP production, and spare respiratory capacity.

In vivo mouse xenografts experiment

The Ethics Committee of the Hospital of Stomatology at Wuhan University (S07921030H) approved the experiment. Female BALB/c nude mice, 4 weeks old, were acquired from the GemPharmatech Laboratory Animal Co. Ltd. (Nanjing, China). The experiment utilized SCC25 cells that were transfected with *CAV2* knockdown lentivirus. The mice were randomly allocated into two groups, each consisting of five. Each mouse was subcutaneously injected with 200 μL of PBS solution containing 1×10^7 tumor cells. The tumor size was assessed at three-day intervals, and the volumes of the tumors were determined using the formula: $(\text{width}^2 \times \text{length})/2$. Following a period of 36 days, the mice were subjected to euthanasia, and subsequently, the tumor tissues were extracted and sent for analysis. All experiments were performed according to the Guide for the Care and Use of Laboratory Animals at Wuhan University.

Hematoxylin and Eosin staining and immunohistochemical staining

Hematoxylin and eosin (HE) staining was done on tissue sections, and immunohistochemistry staining (IHC) experiments were undertaken on both tissue sections and cell samples using a standard streptavidin-peroxidase procedure, as previously described [6]. This process was applied to both tissue sections and cell samples to analyze protein expression. The slides were digitized using the Panoramic DESK digital pathology scanner (3DHISTECH, Budapest, Hungary). Then, CaseViewer 2.4 (3DHISTECH) randomly selected three fields (×20 magnification). Three fields were captured at a magnification of 200× using a microscope (IX83, Olympus) for cell samples. The NIH ImageJ software quantified positive staining with an IHC toolbox plugin designed for DAB-chromogenic IHC. MOD was calculated as MOD = IOD sum/area sum (IOD: integrated optical density; IOD sum: cumulative IOD of targeted areas in one photo; area sum: sum of targeted areas in the same photo). The antibodies utilized in this work were listed in Supplementary files Table S4.

Luciferase reporter assay

The pGL4-basic plasmid with the *CAV2* promoter (pGL4-*CAV2* promoter), the pGL4-basic luciferase plasmid, pcdna3.1-*PPARG* plasmid, pcdna3.1-basic plasmid, and the RL-TK plasmid were acquired from GenePharma. Cells were co-transfected with pGL4-*CAV2* promoter plasmids and RL-TK plasmids, along with either pcdna3.1-*PPARG* plasmid or pcdna3.1-basic plasmid using Lipofectamine™ 3000 (Invitrogen, Carlsbad, CA, USA) to investigate the regulation of the *CAV2* promoter by PPARγ. Additionally, to assess the effect of the PPARγ inverse agonist T0070907 on *CAV2* promoter activity, cells transfected with pGL4-*CAV2* promoter plasmids and RL-TK plasmids were pretreated with T0070907 (MCE, Shanghai, China) or DMSO. The cells transfected with the RL-TK plasmid and pGL4-basic luciferase plasmid served as negative controls. After twenty-four hours, the level of luciferase activity was measured using the Luciferase Assay System Kit (Promega, Madison, Wisconsin, USA) following the instructions provided by the manufacturer.

Co-IP

Co-IP experiments were performed using the methods reported in a prior study [22]. The SCC25 cells were lysed using IP lysis buffer (Beyotime) supplemented with a protease inhibitor cocktail (MCE). The whole cell extracts were overnight incubated with PPARγ antibody, NCOR1 antibody, or IgG Rabbit antibody using protein A/G beads (Selleck, Houston, TX, USA) at 4℃. Eventually, the immunocomplex was applied for western blot (WB) analysis. The antibodies for WB were CAV2 antibody, NCOR1 antibody, PPARγ antibody, and GAPDH antibody. Details on the antibodies utilized in this experiment were found in Supplementary files: Table S4.

Statistical analysis

Data were presented as the mean ± SD from at least three independent runs. All statistical analyses were carried

out using GraphPad Prism. The Shapiro-Wilk test of normality (with a *P*-value > 0.05) was employed to assess the normal distribution of the continuous variables before conducting any analysis. The F-test assessed the variance between the groups. The *P* values were calculated using unpaired students' t-test, one-way ANOVA, Wilcoxon test, Mann-Whitney U test, and Kruskal-Wallis H test, as specified in the figure legends. The Bonferroni's test was conducted for *post hoc testing*. The IC_{50} values of T0070907, which represent the concentration of the medication that inhibits 50% of cells, were determined using non-linear regression analysis (curve fitting). A *P*-value < 0.05 was deemed to be statistically significant.

Results

CAV2 was upregulated in OSCC and correlated with poor clinical outcomes

Firstly, *CAV2* expression was significantly higher in OSCC samples than in normal tissues (Fig. 1A). Subsequent examination revealed that increased *CAV2* expression was linked to a worse prognosis with both overall survival and disease-specific survival among patients (Fig. 1B and C). The expression of *CAV2* decreased as lymph node metastasis progressed, and the mRNA levels of *CAV2* in N3 individuals were considerably reduced compared to N1 and N2 individuals (Fig. 1F). *CAV2* was independent of clinical T stage, histologic grade, clinical M stage, age, and gender (Fig. 1D, E and G-I). Furthermore, HNSC_GSE103322 of the TISCH database was used to evaluate *CAV2* expression in HNSCC tumor microenvironment. In the HNSC_GSE103322 dataset, eleven cell types were found, with the highest number of 2488 malignant cells (Fig. 1J and K). *CAV2* was highly expressed in malignant cells (Fig. 1L). Analyses showed that OSCC cell lines CAL27, SCC25, and SCC9 had higher *CAV2* mRNA expression levels compared to the normal oral epithelial cell line OKF4 (Fig. 1M). CAV2 protein expression was also upregulated in CAL27 and SCC25 (Fig. 1N and O). The results mentioned above generally indicated that CAV2 was upregulated in OSCC and predicted poor clinical outcomes.

Downregulation of *CAV2* in OSCC inhibited cell proliferation and promoted apoptosis

Lentiviral transduction systems inhibited its expression in SCC25 and CAL27 cells (Fig. S1). KD and KD-2 effectively reduced the expression of *CAV2* mRNA and CAV2 protein, respectively, compared to the corresponding negative control NC and NC-2 (Fig. 2A and B). SCC25 and CAL27 cells transfected with KD and NC were selected for experiments. Following *CAV2* inhibition, there was a noticeable decrease in the proliferation rate of SCC25 and CAL27 cells (Fig. 2C and D). Additionally, the ability of OSCC cells to form colonies was significantly reduced upon *CAV2* knockdown (Fig. 2E and F). Down-regulation of *CAV2* blocked DNA replication in SCC25 cells and CAL27 cells, respectively (Fig. 2G and H). Moreover, *CAV2* knockdown in OSCC cells increased apoptosis (Fig. 2I and J). Next, RNAseq analyses were performed on SCC25 NC and SCC25 KD cells (Fig. S2A-S2C). The numbers of the DEGs, SCC25 KD versus SCC25 NC, were 2889 (51% down) and 2748 (49% up) (Fig. S2D-S2E)—all the genes with Q values ≤ 0.05 and dropped the log_2FC cutoff requirement. Moreover, RNAseq highlighted an enrichment in apoptosis and MAPK signaling pathway (Fig. 2K). Furthermore, the *CAV2* knockdown group exhibited increased mRNA expression of *JUN*, *Cytochrome c (CYTO C)*, and *CAS9* and decreased expression of *BCL2* relative to the control group in CAL27 cells (Fig. 2L). Moreover, further examination uncovered increased amounts of CAS9, CAS3, c-JUN, and CYTO C, decreased p44/42 MAPK (Erk1/2), and BCL2 protein in the *CAV2* knockdown group compared to the control group (Fig. 2M and N). The results indicated that *CAV2* knockdown suppressed proliferation and enhanced apoptosis, potentially through the MAPK signaling pathway in OSCC cells.

CAV2 regulated the LD dynamics in OSCC

LD accumulation was markedly higher in SCC25 and CAL27 cells than in OKF4 cells (Fig. S3). The data here aligned well with our previous conclusions [5]. According to the Human Protein Atlas, CAV2 is predicted to localize in the cytoplasm and cell membrane. Our fluorescence microscopy results consistently showed CAV2 expression in both the cytoplasm and cell membrane of SCC25 and CAL27 cells (Fig. 3A). CAV2 protein was localized in the LDs in SCC25 and CAL27 cells (Fig. 3A and B). To further investigate the role of CAV2 in LD dynamics and the colocalization of CAV2 with LDs, the overexpression virus was constructed and transfected to upregulate CAV2 expression in SCC25 and CAL27 cells (Fig. S4A and S4B). Meanwhile, the results indicated that exogenous CAV2 increased LDs, and the CAV2 coated the LDs in OSCC cells (Fig. 3C and D, S4C, and S4D). The co-localization of CAV2 protein to LDs was not influenced by increasing the levels of CAV2, as indicated by Pearson's Correlation coefficients ranging from 0.5 to 1 (Fig. 3C and D). Following CAV2 overexpression, LD accumulation was risen, and LDs remained smaller. LD accumulation dropped after CAV2 knockdown compared to control cells, and LDs stayed larger (Fig. 3E and F). After KEGG biological process analysis, the GO Cellular Component terms enriched in LD were found and exhibited in terms of the heat map (Fig. S4E), which supported that the knockdown of CAV2 led to the alteration of intracellular LD metabolism. Thus, the data demonstrated that CAV2 directly influenced LD accumulation,

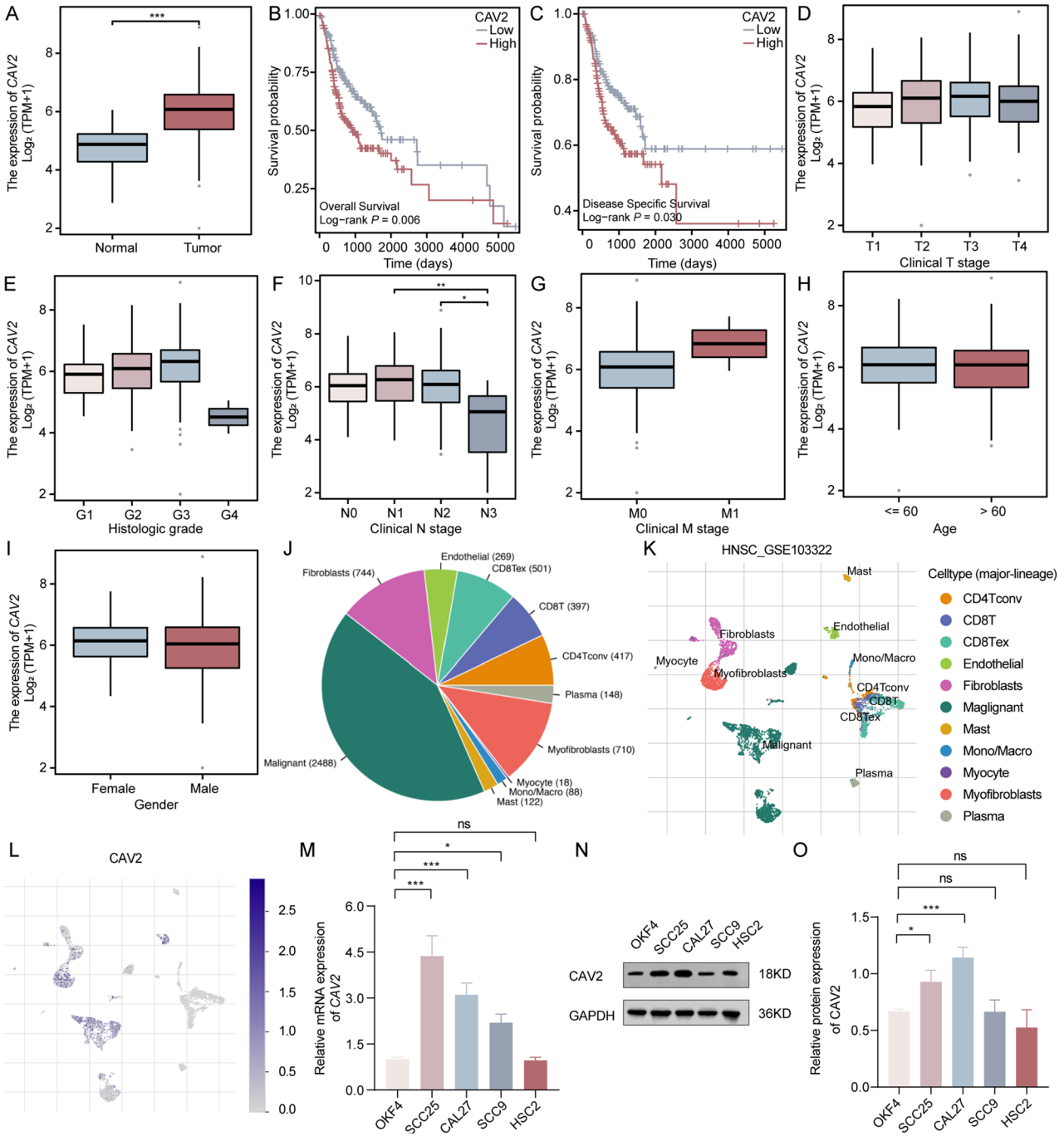

Fig. 1 CAV2 was upregulated in OSCC and correlated with poor clinical outcomes. (**A**) Expression levels of *CAV2* in OSCC (n=330) compared to normal samples (n=32) were analyzed using RNA sequencing data from TCGA. (**B**-**C**) Kaplan-Meier survival analysis of overall survival (**B**) and disease-specific survival (**C**) stratified by high and low *CAV2* expression in OSCC patients. (**D**-**I**) *CAV2* expression in OSCC of different clinical T stage, histologic grade, clinical N stage, clinical M stage, age, and gender. n=320, 322, 316, 313, 329, 330. (**J** and **K**) The cell types and their distribution in HNSC_GSE103322 datasets. (**L**) Distribution of *CAV2* in different cells in HNSC_GSE103322 datasets. (**M**-**O**) CAV2 expression in OSCC and normal oral keratinocyte cell lines. mRNA levels were measured by RT-qPCR (**M**), protein levels by Western blot (**N**), and quantified in (**O**). (**A**, **D**-**I**) Data were overlaid by the median and IQR. (**B**-**C**) Data were presented as cumulative survival curves. (**M**-**O**) Data were represented as mean ± SD of three independent experiments. Significance was determined by the Wilcoxon rank sum test (**A**, **H**), the Logrank test (**B**-**C**), the Kruskal-Wallis test with Dunn's multiple comparison tests (**D**, **E**), Welch t' test (**I**), Welch one-way ANOVA test with a post-hoc Games-Howell (**F**), one-way ANOVA (**M** and **O**). *$P < 0.05$, **$P < 0.01$, ***$P < 0.001$, ns: no significance. CAV2: C aveolin2; OSCC: oral squamous cell carcinoma; TCGA: T he Cancer Genome Atlas; RT-qPCR: real-time quantitative polymerase chain reaction; IQR: interquartile range

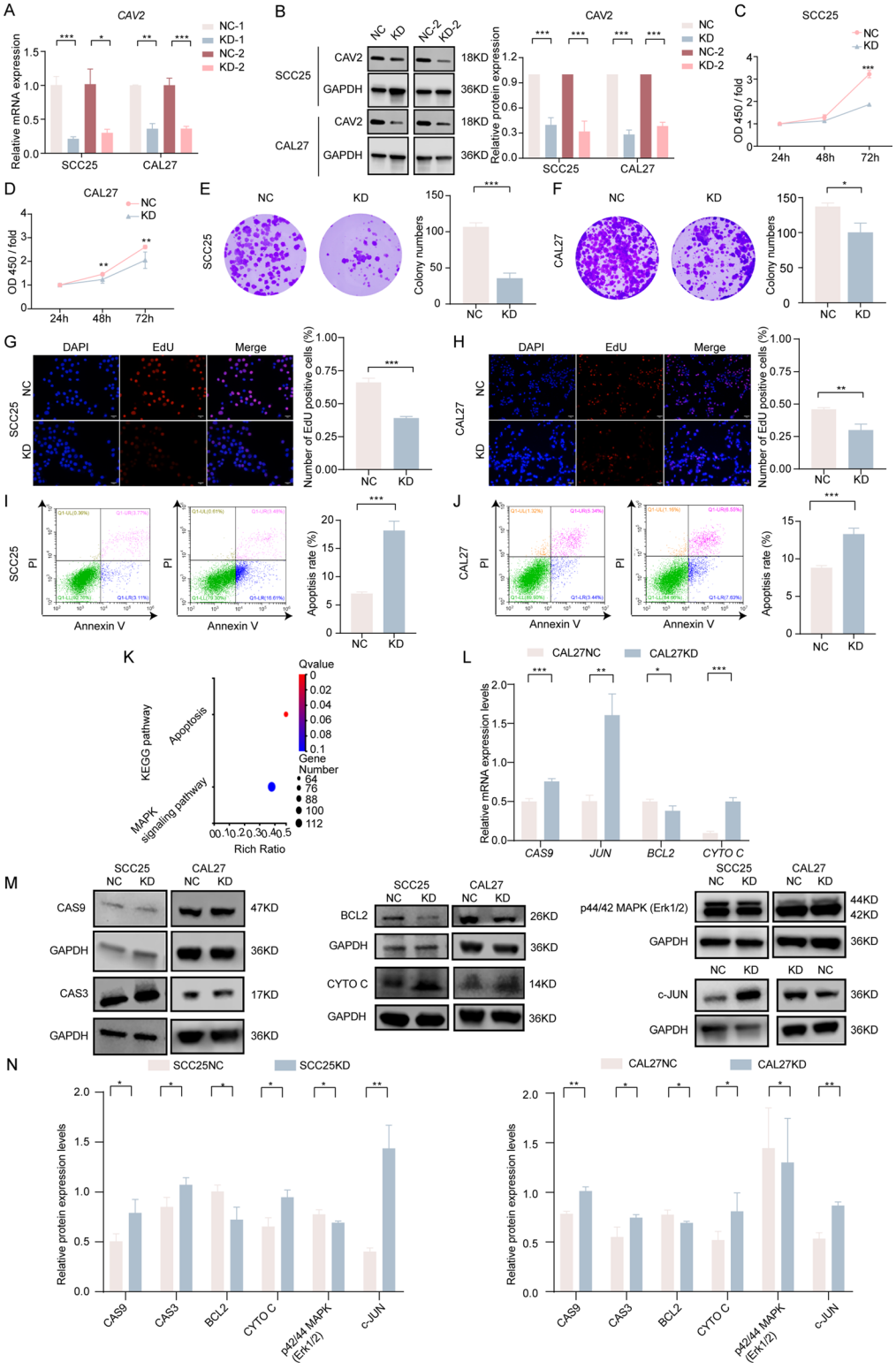

Fig. 2 (See legend on next page.)

(See figure on previous page.)

Fig. 2 Downregulation of *CAV2* in OSCC inhibited cell proliferation and promoted apoptosis. (**A**) Validation of *CAV2* knockdown in SCC25 and CAL27 cells using shRNA targeting *CAV2* (KD) or scrambled control shRNA (NC), both labeled with GFP for green fluorescence tracking. For additional validation, KD-2 and NC-2 groups were established using a second shRNA sequence targeting *CAV2* (KD-2) and its respective scrambled control (NC-2), both labeled with RFP for red fluorescence tracking. mRNA expression was measured by RT-qPCR (**A**), and protein levels were assessed by Western blot (**B**). (**C** and **D**) Cell proliferation was measured by growth curve analysis over 72 h. Cells were seeded in 96-well plates and analyzed at 24 h intervals using a CCK-8 assay. (**E** and **F**) Colony formation assay showing reduced clone formation after *CAV2* knockdown. Cells were seeded in 6-well plates and cultured for 14 days before staining with crystal violet. (**G** and **H**) EdU proliferation assay of SCC25 and CAL27 cells stably expressing KD or NC, respectively. Representative images of EdU labeling (red) and DAPI (blue) staining were shown. Quantification of the percentage of EdU-positive cells was calculated as follows: EdU-positive cell numbers (red dots)/total numbers (blue dots) ×100%. Scale bars of (**G**) = 20 μm, Scale bars of (**H**) = 50 μm. Five visual fields per sample were randomly selected for statistical analysis. (I and J) The apoptosis of SCC25 and CAL27 cells stably expressed KD or NC was measured by flow cytometry using APC Annexin V/PI apoptosis detection, respectively. Quantitative analysis of apoptosis rate. (**K**) KEGG pathway enrichment bubble charts displayed pathways involved in apoptosis and MAPK signaling. (**I**) Quantifying *CAS9*, *JUN*, *BCL2*, and *CYTO C* mRNA expression in CAL27 cells treated with shRNA targeting CAV2 (KD) or scrambled control shRNA (NC). (**J** and **K**) Protein expression and quantification of CAS9, CAS3, BCL2, CYTO C, p44/42 MAPK (Erk1/2), and c-JUN in SCC25 and CAL27 cells transduced with shRNA targeting CAV2 (KD) or scrambled control shRNA (NC). All data were expressed as the mean ± SD (n≥3). Significance was determined by the Student's t-test (A-J, L, and N). **P*<0.05, ***P*<0.01, ****P*<0.001. CAV2: Caveolin2; OSCC: oral squamous cell carcinoma; RT-qPCR: real-time quantitative polymerase chain reaction; KD: shRNA targeting *CAV2*, labeled with GFP for green fluorescence tracking; NC: scrambled control shRNA, labeled with GFP for green fluorescence tracking; KD-2: shRNA targeting *CAV2*, labeled with RFP for red fluorescence tracking; NC-2: scrambled control shRNA, labeled with RFP for red fluorescence tracking; CCK8: Cell Counting Kit 8; EdU: 5-ethynyl-2′-deoxyuridine; DAPI: 4′,6-diamidino-2-phenylindole; CAS9: Caspase9; CAS3: Caspase3; CYTO C: Cytochrome C

size, and colocalization with LDs in OSCC cells, suggesting a potential role for CAV2 in lipid metabolism regulation.

Gene Inhibition of *CAV2* altered lipid profiles and induced PUFA accumulation in OSCC

Building on our discovery, the lipid alternations caused by CAV2 in OSCC cells were investigated more thoroughly using lipidomic analysis. Quality control samples were employed to validate the performance of the LC-MS platform before and after analyzing each block, ensuring the acquisition of high-quality data (Fig. S5A). Next, the samples underwent qualitative analysis. Base peak chromatograms were compared with normal control after applying knockdown *CAV2* to SCC25 cell samples (Fig. S5B) and the chromatographic peak response strength and retention time of distinct samples partially overlapped in the data, suggesting comparability between the two sets of samples. Unsupervised PCA was used to visually and intuitively examine the impact of *CAV2* knockdown in SCC25 cells. QC samples that clustered together exhibited good data quality (Fig. S5C). The OPLS-DA method was employed to analyze variables exhibiting notable micromolecule alterations within each group. The gathered results indicated that the samples could be effectively classified and characterized (Fig. S5D). The model's accuracy was additionally evaluated using a permutation test. The parameters of the OPLS-DA score plot obtained from these two groups were $R^2Y(cum) = 0.95$ and $Q^2(cum) = 0.067$, which indicated excellent fitness and acceptable reliability (Fig. S5E) and suggested that the model could be used for subsequent lipid metabolism analysis [43].

First, a volcano plot was drawn to visualize the variation of differential lipids after the knockdown of CAV2 in SCC25 cells (Fig. S5F). Next, a heat map was created to depict the distribution of different lipids (Fig. 4A). Specifically, there were 69 differential lipids with 46 lipids up and 23 lipids down between the SCC25NC group and SCC25KD group: 12 for phosphatidylcholine (PC), 9 for phosphatidylethanolamine (PE), 7 for phosphatidylinositol (PI) and (O-acyl)-1-hydroxy fatty acid (OAHFA), 6 for sphingomyelin (SM) and phosphatidylglycerol (PG), 5 for monogalactosyldiacylglycerol (MGDG), 4 for lysophosphatidylcholine (LPC) and FA, 3 for phosphatidylserine (PS) and phosphatidylethanol (PEt), 1 for phosphatidic acid (PA), dimethylphosphatidylethanolamine (dMePE) and diglyceride (DG) (Fig. S5G and Fig. 4A). The *CAV2* knockdown significantly promoted the accumulation of DG, FA, and OAHFA. On the other hand, the other lipid composition of OSCC cells was also altered, with increasing dMePE, PA, PS, PG, PEt, LPC, and MGDG and decreasing PC, PI, SM, and PE detected (Fig. 4B). The phenomenon of disrupted lipid homeostasis after knockdown of *CAV2* using summary diagrams (Fig. 4C).

KEGG pathway enrichment analysis of lipid-related differential pathways revealed a significant upregulation, particularly in pathways associated with the regulation of lipolysis in adipocytes, linoleic acid metabolism, choline metabolism in cancer, and the biosynthesis of polyunsaturated fatty acids (PUFAs) (Fig. 4D). Lipidomic studies also highlighted the formation of enhanced PUFA biosynthesis, including FA(20:5), FA(20:4), FA(22:5), and FA(24:6) after the knockdown of *CAV2* in SCC25 cells (Fig. 4E). Furthermore, the Pearson correlation analysis revealed that differential PUFAs were positively correlated with differential lipids, including LPC, FA, OAHFA, dMePE, PC, MGDG, PI, PS, PE, PG, and PEt, and negatively correlated with SM (Fig. 4F). Complex relationships between differential PUFAs and multiple differential lipid components might have profound implications for disturbed lipid homeostasis mediated by *CAV2* in OSCC. Overall, the knockdown of *CAV2* led to significant disruptions in lipid homeostasis, characterized by

the accumulation of DG, FA, and OAHFA, along with alterations in the composition of various lipid classes and a notable upregulation in PUFA biosynthesis in OSCC cells.

CAV2-knockdown generated a multi-gene regulatory network that influenced PUFA accumulation, potentially targeting mitochondria in OSCC

The differential lipids and genes between each comparison group in the single omics were shown in Table S6 and S7, which were visualized using the volcano plot (Fig. S6A and S6B). The multivariate unsupervised model can reveal the regularity of the two data sets at the overall level, which is better than single-omics data [40]. The PCA was used to analyze the gene and lipid data separately, and then, datasets were combined to compare the differences between SCC25KD and SCC25NC better. The results indicated that the SCC25KD group could be effectively classified and characterized (Fig. S6C-S6E). The rCCA was conducted to uncover shared factors of variation across SCC25KD and SCC25NC cells and then used to integrate lipidomics and transcriptomics data sets [40]. Correlation circle plots further emphasized the relationships between DEGs and lipids that show differential expression (Fig. S6F). Correlation coefficients ≥ 0.9 were displayed as the Circos plot in Fig. S6G, showing that differential gene transcription was closely linked to the differential lipid variation in gene-lipid interaction networks mediated by CAV2 in OSCC cells.

Applying the top20 chord plots of rCCA correlations between differential genes and lipids with a correlation cutoff of 0.9958, pairs of candidate genes and lipids were identified that were directly mechanistically related (the gene coding for an enzyme which directly regulated the reaction involving its paired lipids) (Fig. 5A). Several significant correlations were identified in the analysis of gene-lipid interactions, elucidating potential regulatory networks within the cellular milieu (Fig. 5A and B). The FA 20:4 was observed to be positively correlated with a cluster of genes, namely *ATP8A1*, *SLC29A4*, *SERPINA5*, *CAMK2B*, *KRT23*, *ADAMTSL4*, *PECAM1*, and *DAAM2*, which suggested that these genes might coordinately modulate FA (20:4) levels or activity, implicating a multigene regulatory mechanism. Similarly, OAHFA (42:8) demonstrated a positive correlation exclusively with the *ATP8A1* gene, indicating a specific interaction or regulatory relationship between this unique lipid species and the *ATP8A1* gene. The FA (24:6) exhibited positive correlations with an array of genes, including *HLA-DPA1*, *CDC42EP5*, *MYH14*, *GSTM4*, *KLK8*, *SERPING1*, *NTN4*, *CCNL1*, and *PADI3*. This diversified gene set implied a broader regulatory spectrum influencing the levels or activities of FA (24:6). FA (20:5) was positively correlated with *GABRP*, suggesting a potential functional or regulatory linkage between this FA and the *GABRP* gene. Contrastingly, a negative correlation was noted between PC(29:1)(rep) and the *CEL* gene, signifying an inverse relationship in the regulation or activity between this lipid species and the *CEL* gene. The number of pathways enriched in the gene circle was 233, and that in the lipid circle was 22. The number of pathways common to both omics datasets was 21 (Fig. 5C). Notably, the pathways related to lipid metabolism enriched by the KEGG pathway were regulation of lipolysis in adipocytes, linoleic metabolism, glycerophospholipid metabolism, choline metabolism in cancer, and arachidonic acid metabolism (Fig. 5D).

The interaction and regulation of these metabolic pathways in cells involved multiple organelles, including LDs, mitochondria, etc. CPT1A acts on the outer mitochondrial membrane to convert FAs into the corresponding carnitine esters. FAs can traverse the outer layer of the mitochondrial membrane and enter into the inner compartment of the mitochondria by this mechanism [44]. The docking results were displayed in the supplementary files: Table. A binding affinity of -5 kcal/mol or less was crucial. The FA(20:4) and FA(24:6) results exhibited good binding properties. The FA(20:5) and FA(22:5) results had a particular binding affinity. Then, we used the visualization method shown in Fig. 5E and H to visualize the specific binding of FA(20:4) to the Asp 20 and Arg 22 via H donor and H acceptor, FA(20:5) to the Leu 23 via H donor and H acceptor, FA(22:5) to the His 25 via H-pi, and FA(24:6) to the GLU 3 via H donor. Compared to the control group, the *CAV2* knockdown group exhibited higher expression levels of the CPT1A protein (Fig. 5I). Moreover, it was discovered that DEGs were enriched in the GO cellular component category associated with mitochondria structure and function in SCC25 cells with the *CAV2* knocked down (Fig. 5J). The above results implied that the accumulated PUFAs would likely flow to the mitochondria. These findings revealed a complex CAV2-mediated gene-lipid interaction network in OSCC, particularly involving PUFAs, suggesting intricate regulatory mechanisms in lipid metabolism and cell signaling.

Gene Inhibition of *CAV2* promoted lipolysis in OSCC

The inhibition of *CAV2* increased glycerol release in SCC25 and CAL27 cells (Fig. 6A). After *CAV2* knockdown, a significant increase in p-HSL protein levels was detected in OSCC cells. In the CAL27 cell line, total HSL levels were increased, while no significant change in HSL protein expression was observed in SCC25 cells. Moreover, *CAV2* suppression decreased the basal expression of the lipolysis-related protein PLIN3 by 13.04% ± 0.05% in SCC25 cells and 25.73% ± 0.04% in CAL27 cells (Fig. 6B). Moreover, the inhibition of *CAV2* led to a

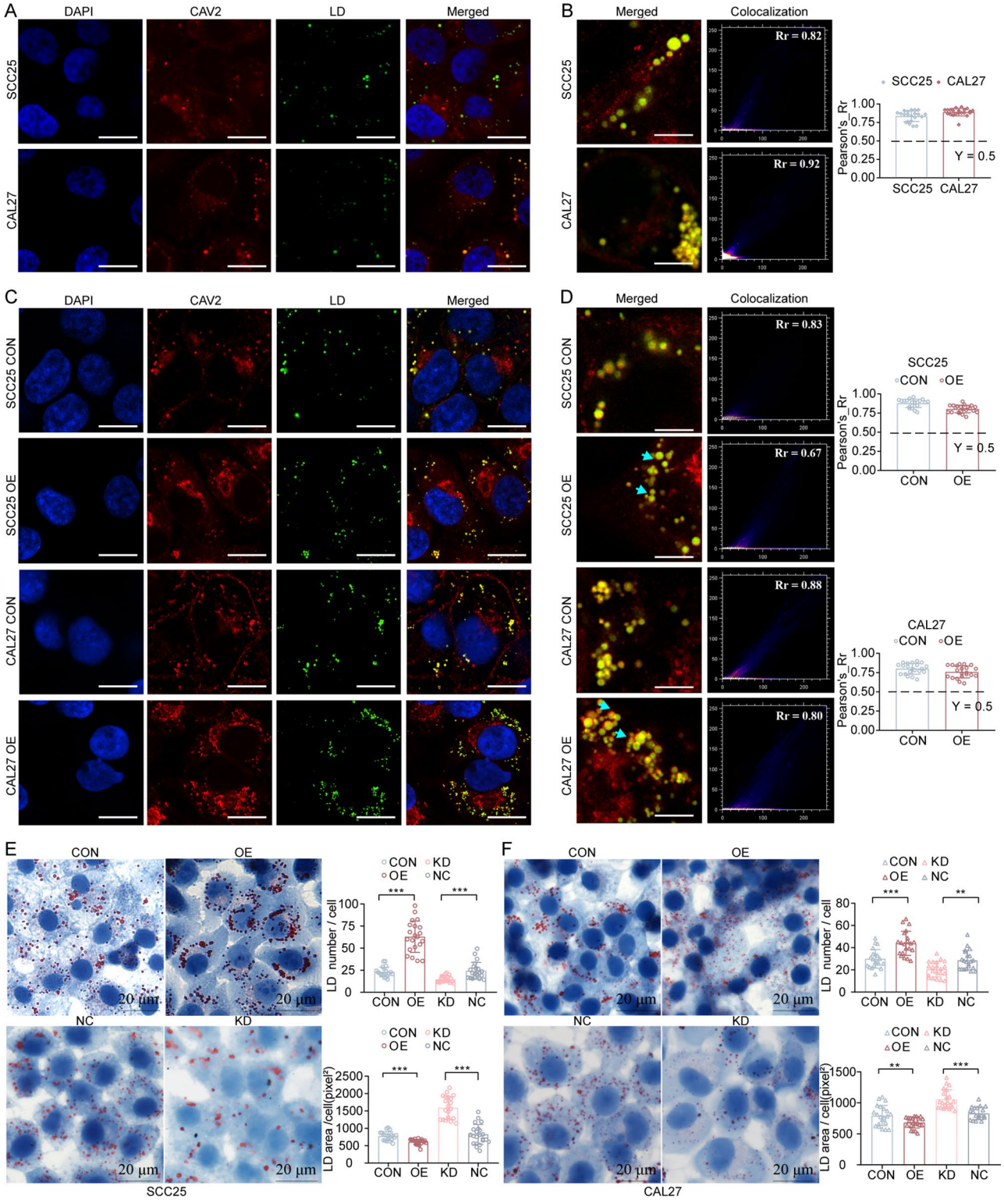

Fig. 3 (See legend on next page.)

1.42 ± 0.12 fold and 1.22 ± 0.06 fold increase in lipolysis-related gene *LIPE* mRNA expression in SCC25 cells and CAL27 cells, respectively. The inhibition of *CAV2* led to a rise in *PNPLA2* mRNA expression in CAL27 cells. However, there was no significant change in the expression of *MGLL* mRNA (Fig. 6C and D). The suppression of *CAV2* increased HSL protein expression in SCC25 and CAL27 cells (Fig. 6E and F). TEM indicated that the

(See figure on previous page.)

Fig. 3 CAV2 regulated LD dynamics in OSCC. (**A**) IF staining was performed to observe the expression of CAV2 protein (red) in SCC25 and CAL27 cells. The expression of CAV2 protein (red) was detected using anti-CAV2 antibodies, while LDs were stained with BODIPY™ 493/503 (green), and nuclei were counterstained with DAPI (blue). Confocal microscopy images revealed CAV2 localization in the cytoplasm and cell membrane, with co-localization between CAV2 and LDs observed as yellow regions in the merged images. Scale bar = 10 μm. (**B**) Co-localization of CAV2 with LDs was further demonstrated in representative high-magnification images. Co-localization was quantified using Pearson's correlation coefficients (values between 0.5 and 1 indicate significant co-localization), calculated with ImageJ software. Seven randomly selected visual fields per sample were analyzed statistically. Scale bar = 4 μm. (**C**) Representative IF and BODIPY™ 493/503 staining images of SCC25 and CAL27 cells with CAV2 OE and respective CON groups. Nuclei were stained with DAPI (blue), LDs with BODIPY™ 493/503 (green), and CAV2 protein with anti-CAV2 antibodies (red). Scale bar = 10 μm. (**D**) High-magnification images of CAV2 and LD co-localization in CON and OE OSCC cells. Scale bar = 4 μm. Pearson's correlation coefficients for co-localization were calculated for CON and OE cells, with seven visual fields per sample analyzed. (**E** and **F**) Representative images and quantitative analysis of LD number and area per cell in SCC25 and CAL27 cells subjected to CON, OE, KD, and NC treatments. LD staining was performed using Oil Red O assay. LD dynamics were quantified after 48 h of culture, with seven visual fields analyzed per sample. Scale bars = 20 μm. All data were expressed as the mean ± SD ($n \geq 3$). Significance was determined by the Student's t-test (E-F). $^{**}P<0.01$, $^{***}P<0.001$. CAV2: Caveolin2; LD: lipid droplet; OSCC: oral squamous cell carcinoma; IF: immunofluorescence; OE: CAV2 overexpression using lentiviral-mediated overexpression (no fluorescence labeling); CON: control using lentiviral-mediated empty vector (no fluorescence labeling); KD: shRNA targeting CAV2, labeled with GFP for green fluorescence tracking; NC: scrambled control shRNA, labeled with GFP for green fluorescence tracking; DAPI: 4′,6-diamidino-2-phenylindole

downregulation of *CAV2* in OSCC cells contributed to forming LDs-lysosome contacts, which once again confirmed the CAV2-mediated lipolytic activation (Fig. 6G and H). Therefore, CAV2 notably influenced the metabolism of OSCC cells, particularly in regulating lipolysis.

Knockdown of *CAV2* caused mitochondrial dysfunction in OSCC

Our study suggested a notable decrease in critical mitochondrial functions, such as oxidative phosphorylation, the citrate cycle, and activities of mitochondrial respiratory chain complex I and the overall respiratory chain, as detailed in Fig. S7A-S7C. Following this, a reduction was observed in ROS in OSCC cell lines treated with shCAV2 compared to the vehicle control, as evidenced by the decreased green fluorescence in the diagrams (Fig. 7A). MMP was also diminished in the *CAV2* knockdown cells compared to control cells, reflecting a reduction in high mitochondrial membrane potential (Fig. 7B). Non-mitochondrial oxygen consumption showed no significant difference between KD and NC groups, suggesting that the observed changes were specific to mitochondrial respiration rather than extramitochondrial oxygen utilization. In both cell lines, *CAV2* knockdown significantly decreased basal respiration, maximal respiration, proton leak, and ATP production, indicating impaired mitochondrial function, reduced respiratory reserve, compromised mitochondrial membrane integrity, inefficiency in maintaining the proton gradient, and diminished ATP production capacity (Fig. 7C and D). Furthermore, a reduction in spare respiratory capacity was specifically observed in SCC25 cells, suggesting a potential impairment in their ability to adapt to increased energy demands during rapid proliferation. In contrast, no significant difference in spare respiratory capacity was detected in CAL27 cells (Fig. 7C and D). Furthermore, a comparison with the control cells showed a decrease in mitochondrial staining intensity after *CAV2* knockdown (Fig. 7E and F), further indicating mitochondrial dysfunction following *CAV2* interference in OSCC. *CAV2* knockdown also resulted in abnormal mitochondrial morphology, with mitochondria appearing elongated and fragmented in the knockdown group compared to the disc-shaped mitochondria observed in the control group (Fig. 7G and H). RNA sequencing analysis showed enrichment in KEGG pathways related to lysosomes and mitophagy (Fig. 7I). TEM analysis revealed that treatment with shCAV2 increased mitochondria targeting lysosomes, signifying induced mitophagy in OSCC cells (Fig. 7J and K). In summary, *CAV2* knockdown led to mitochondrial dysfunction by disrupting mitochondrial structure or function, destabilizing electron transport chain complexes, resulting in reduced electron transport efficiency, decreased ROS and MMP, impaired ATP synthesis, and lower proton leak.

Knockdown of *CAV2* inhibited OSCC progression in vivo

In a mouse model, cells with reduced *CAV2* expression demonstrated a markedly diminished capability for tumor formation (Fig. 8A). Comparing the *CAV2* knockdown group to the negative control showed a notable decrease in tumor volume and weight (Fig. 8B - D). Histological analysis of mouse tumors revealed a proliferation of apoptotic neoplastic cells and vacuole-like formations in the *CAV2* knockdown samples (Fig. 8E). Tumor specimens from the *CAV2* knockdown group demonstrated decreased LD accumulation (Fig. 8F). Furthermore, tumor samples from the *CAV2* knockdown group exhibited a reduction in the levels of Ki67 and PLIN3, alongside a rise in the expression of CAS3, CAS9, HSL, and CPT1A (Fig. 8G). Data analyses revealed a positive correlation between *CAV2* expression and the levels of *PLIN3* and *CAS3*, alongside a negative correlation with *LIPE* and *BCL2* expressions. Additionally, no significant association was observed with *PNPLA2* and *CAS9* (Fig. S8A-S8F). The results demonstrated that *CAV2* knockdown prohibited OSCC progression in vivo in the mouse model while inducing apoptosis, promoting LD-mediated lipolysis, and leading to mitochondrial dysfunction.

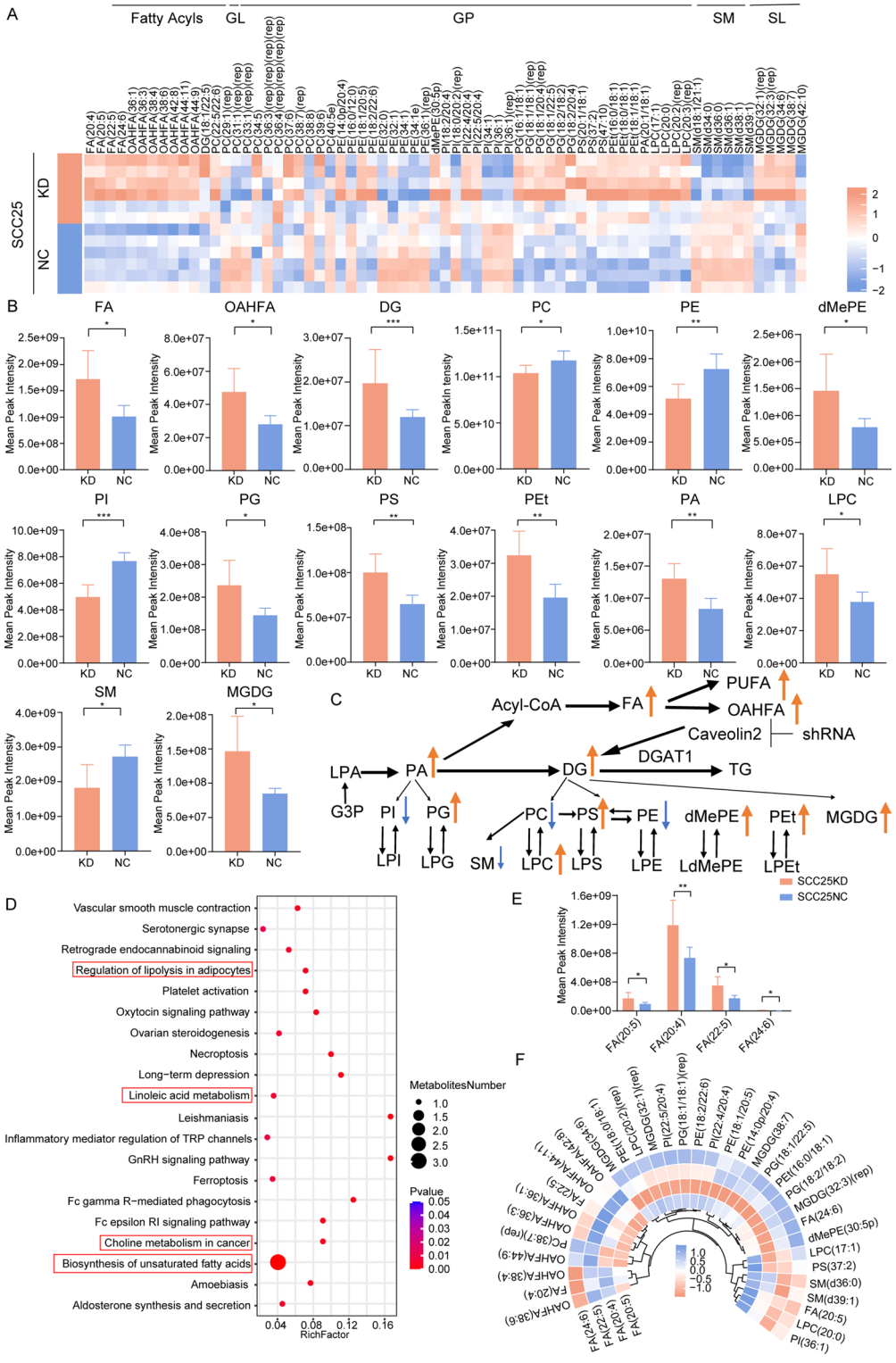

Fig. 4 (See legend on next page.)

Dysregulated transcriptional repression of CAV2 by PPARγ in OSCC

The correlation analysis acquired from TCGA revealed that *PPARG* expression was inversely correlated with *CAV2* and *PLIN3* and directly correlated with *LIPE*, *MGLL*, and *BCL2* expression (Fig. 9A-E). These correlations proposed that *PPARG* might act as a critical transcriptional regulator, influencing CAV2's role

(See figure on previous page.)

Fig. 4 Gene inhibition of CAV2 altered lipid profiles and induced polyunsaturated fatty acids (PUFAs) accumulation in OSCC. (**A**) Heatmap for the differential expression lipids in SCC25 KD versus NC cells ($n = 6$ per group). (**B**) Statistical chart of lipid sub-classes and the corresponding number of lipid molecules in SCC25 KD and SCC25 NC cells (mean ± SD, $n = 6$). (**C**) Summary diagram of lipid changes. Levels of representative individual lipid species in SCC25 KD and NC cells. (**D**) Bubble chart of metabolic pathway enrichment. (**E**) Levels of differential PUFAs in SCC25 KD and NC cells. (**F**) Related heatmaps of differentially expressed FAs and other differentially expressed lipids. Significance was determined by the Student's t-test (**B** and **E**). Correlation analysis was performed using Pearson correlation analysis (**F**). *$P<0.05$, **$P<0.01$, ***$P<0.001$. CAV2: Caveolin2; OSCC: oral squamous cell carcinoma; PUFAs, polyunsaturated fatty acids; KD: shRNA targeting CAV2, labeled with GFP for green fluorescence tracking; NC: scrambled control shRNA, labeled with GFP for green fluorescence tracking; GL, glycerolipids; GP, glycerophospholipids; SP, sphingolipids; SL, saccharolipids; OAHFA, (O-acyl)-1-hydroxy fatty acid; FA, fatty acid; DG, diglyceride; PC, phosphatidylcholine; PE, phosphatidylethanolamine; dMePE, dimethylphosphatidylethanolamine; PEt, phosphatidylethanol; PS, phosphatidylserine; PI, phosphatidylinositol; PG, phosphatidylglycerol; PA, phosphatidic acid; LPC, lysophosphatidylcholine; SM, sphingomyelin; MGDG, monogalactosyldiacylglycerol

in lipolysis, mitochondrial dysfunction, and apoptosis. Analyzed using predictive modeling, a possible PPARγ binding site was found in the promoter region of CAV2, indicating a direct regulatory connection (Fig. 9F and G, and supplementary files: Table S9). Subsequent reporter assays supported this, showing decreased activity of CAV2 promoter upon PPARγ overexpression in 293T cells, confirming that PPARγ could inhibit the transcription of CAV2 in normal cells (Fig. 9H). However, the result displayed that PPARγ could increase the transcription of CAV2 in OSCC cells (Fig. 9I), which indicated the dysregulated regulation of PPARγ in OSCC. Furthermore, analyses indicated lower *PPARG* mRNA levels in OSCC samples than normal samples (Fig. 9J). Lower expression levels of *PPARG* were associated with poorer overall and disease-specific survival (Fig. 9K and L). Based on the box plot showing higher *PPARG* expression in G3 compared to G1, which suggested that *PPARG* expression was associated with more advanced tumor grade, potentially implicating *PPARG* as a marker of OSCC progression or aggressiveness (Fig. 9M). *PPARG* was independent of clinical T stage, M stage, N stage, age, and gender (Fig. S9A-E). In the HNSC_GSE103322 dataset, *PPARG* was low expressed in malignant cells (Fig. 9N). *PPARG* expression was reduced in the CAL27, SCC25, SCC9, and HSC2 cells compared to the OKF4 cells (Fig. 9O). The SCC25, CAL27, SCC9, and HSC2 cells had higher PPARγ expression than the OKF4 cells (Fig. 9P). Protein-protein interactions prediction showed PPARγ interacted with NCOR1 and CAV2, respectively (Fig. S9F). Experimental confirmed that PPARγ and CAV2 could not coimmunoprecipitate with NCOR1 in OSCC. On the other hand, although PPARγ did not coimmunoprecipitate with NCOR1, it did exhibit a reaction with CAV2 (Fig. 9Q). This interaction pattern supported the notion that the expected recruitment of the NCOR1 corepressor by PPARγ, crucial for transcriptional repression of CAV2, was compromised in OSCC. Consequently, the regulatory control of CAV2 by PPARγ appeared to be disrupted in OSCC.

Enhancing suppression of CAV2 using transcriptional repression of PPARγ promoted cell apoptosis, lipolysis, and mitochondrial dysfunction in OSCC

The PPARγ proteins and the PPARγ inverse agonist T0070907 exhibited good binding properties (Supplementary files: Table S10). Specifically, the specific binding of T0070907 to the Arg 288, Cys 285, and Met 348 amino acids via pi-H, H donor, and H donor and interactions of the PPARγ receptor were visualized (Fig. S10A). Following a 24-hour treatment with T0070907 (25 μM), the expression of CAV2 protein was markedly reduced (Fig. 10A), and CAV2 promoter activity was significantly diminished (Fig. 10B), indicating that T0070907 effectively inhibited CAV2 transcription in OSCC. Furthermore, *CAV2* knockdown reduced the IC_{50} values of T0070907 in SCC25 cells (Fig. 10C and Fig. S10B-C), while no significant effect was observed in CAL27 cells (Fig. 10D and Fig. S10D-E). Downregulation of *CAV2*, in combination with T0070907, further suppressed colony growth (Fig. 2E and F, and 10E) and enhanced apoptosis (Fig. 10F), indicating a synergistic effect in promoting cell death. Moreover, PLIN3 protein expression was significantly diminished after 24 h of treatment with T0070907 (25 μM) (Fig. 10G), suggesting an enhancement in lipolysis. In both SCC25 and CAL27 cells, the combination of *CAV2* knockdown and T0070907 treatment led to increased LD size (Fig. 10H and I). Interestingly, in CAL27 cells, this combination reversed the reduction in LD number caused by *CAV2* knockdown (Fig. 10I). This suggested a cell type-dependent modulation of LD dynamics through T0070907 and *CAV2*. T0070907 treatment increased mitochondrial intensity, counteracting the decrease in mitochondrial activity induced by *CAV2* knockdown (Fig. 7E and F and 10J, and 10K), suggesting that T0070907 can directly induce mitochondrial dysfunction regardless of *CAV2* suppression. Overall, these results demonstrated that T0070907 decreased the expression of CAV2 via PPARγ transcriptional repression, facilitating apoptosis, enhancing lipolysis, and stimulating mitochondrial function in OSCC.

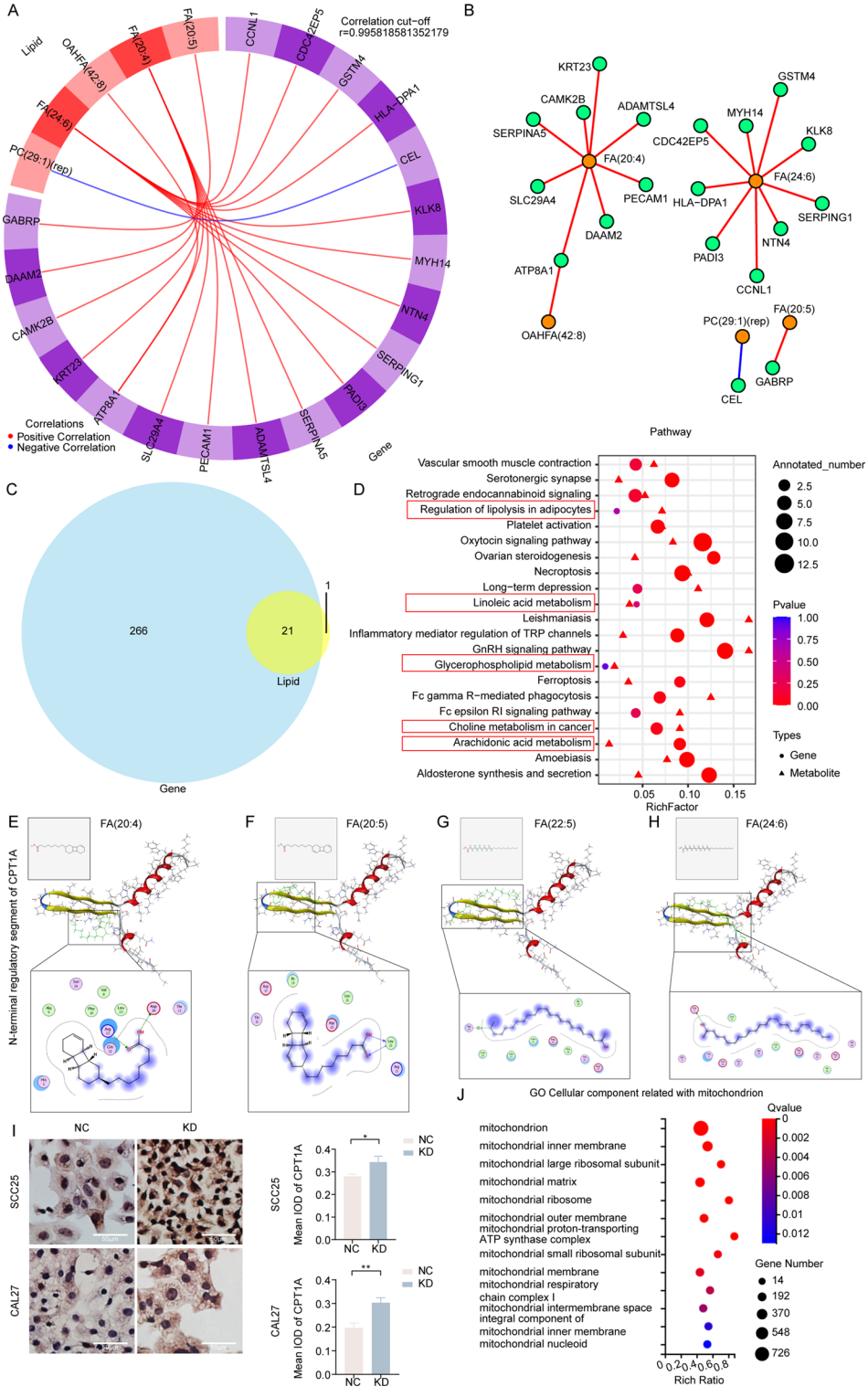

Fig. 5 (See legend on next page.)

Discussion

In this study, CAV2 played crucial roles in OSCC, significantly upregulated, and was associated with poor prognosis. Silencing of *CAV2* decreased cell proliferation and promoted apoptosis potentially through the MAPK signaling pathway in vitro. Notably, CAV2 was targeted to LDs, and its knockdown elevated DG and PUFAs. The regulatory networks of PUFA accumulation in

(See figure on previous page.)

Fig. 5 CAV2 knockdown generated a multi-gene regulatory network that influenced PUFA accumulation, potentially targeting mitochondria in OSCC. (**A**) Chord plots of canonical correlation analysis (CCA) showing correlations between differential genes and differential lipids. The CCA correlation chord diagram was sorted by correlation, and the top 20 pairs with the strongest correlation were selected with a correlation cut-off of 0.9958. Nodes (genes/lipids) were arranged along the circumference, and weighted lines connected nodes. Genes or lipids were on the edge of the circle in the figure, and the connecting line in the circle represented the correlation between genes and lipids; red is a positive correlation, and blue is a negative correlation. Correlation analysis was performed using Spearman correlation analysis. (**B**) Interaction map of the CCA correlation network between differential genes and differential lipids. Each point in the figure represented a gene or a lipid. The more lines between the points, the more genes or lipids it might regulate. Green dots represented genes, yellow dots represented lipids, connecting lines between dots, red lines represented positive correlations, and blue lines represented negative correlations. Correlation analysis was performed by Spearman correlation analysis. (**C**) Venn diagram of differential genes and differential lipids involvement pathways. The numbers in the overlapping area of circles represented the number of pathways that were shared/specific between the two omics. (**D**) Bubble plot of differential gene and differential lipids pathway enrichment analysis. The X-axis is the RichFactor; the larger the value, the greater the ratio of differential genes and differential lipids annotated to the pathway. The triangles in the figure represented functional gene pathways, the circles represented metabolic pathways, the size of the figure represented the number of differential genes and differential lipids annotated to the pathway, and the color represented the significance of the pathway. (**E**-**H**) Molecular docking analysis among the nuclear magnetic resonance (NMR) structure of FA(20:4), FA(20:5), FA(22:5), and FA(24:6) with carnitine O-palmitoyltransferase 1 A (CPT1A), respectively. (**I**) Immunohistochemical analysis of CPT1A in CAL27 and SCC25 cells transduced with CAV2 shRNAs. KD represented cells treated with shRNA targeting CAV2 (labeled with GFP for green fluorescence tracking), and NC represented cells treated with scrambled control shRNA (labeled with GFP for green fluorescence tracking). Mean integrated optical density (IOD) was used to quantify CPT1A protein levels in KD and NC groups. Data were expressed as the mean ± SD (n=3). *P<0.05, **P<0.01. The Student's t-test determined significance. (**J**) The GO Cellular component bubble chart related to mitochondrion with significance. The Q-value is the false discovery rate adjusted P-value. CAV2: Caveolin2; PUFAs: polyunsaturated fatty acids; OSCC: oral squamous cell carcinoma; CCA: canonical correlation analysis; RichFactor: the enrichment factor; NMR: nuclear magnetic resonance; CPT1A: carnitine O-palmitoyltransferase 1 A; KD: shRNA targeting CAV2, labeled with GFP for green fluorescence tracking; NC: scrambled control shRNA, labeled with GFP for green fluorescence tracking; IOD: integrated optical density

CAV2-knockdown OSCC cells were elucidated in detail. Next, the knockdown of *CAV2* promoted lipolysis and compromised mitochondrial function. In vivo, the inhibition of *CAV2* resulted in the suppression of OSCC progression through apoptosis, lipolysis, and mitochondria dysfunction, which was confirmed. Mechanistically, PPARγ unsuccessfully enlisted NCOR1 as a transcriptional repressor to decrease CAV2 in OSCC. Therefore, the T0070907, designed to increase the recruitment of NCOR1, restored the inhibitory effect of PPARγ on *CAV2*, enhancing the therapeutic potential to control OSCC development by promoting apoptosis, lipolysis, and mitochondrion dysfunction mediated by *CAV2* deletion. This study advanced prior work by linking the expression levels of CAV2 to lipid metabolism. This underscores CAV2 as an emerging antineoplastic target.

Studies show higher LD accumulation is connected to OSCC formation and progression [5, 6]. The LD-associated proteins as diagnostic and prognostic markers of tumors have become a hot research topic. CAV2 has been involved in the etiopathogenesis of pancreatic cancer, renal cell carcinoma, and head and neck cancer, and its expression in these cancers is often significantly increased [12, 45, 46]. Our previous study has shown that the CAV2 protein affects the prognosis of OSCC [6]. According to the mRNA expression analysis conducted in this study, *CAV2* was increased in both OSCC tissues and cells. Furthermore, the comparative prognostic data of individuals with OSCC indicated that an elevated level of *CAV2* was associated with a more unfavorable outcome. The above evidence indicated that *CAV2* might be used as a tumor promoter in OSCC. In addition, increased expression of *CAV2* in myofibroblasts stated the critical role of CAV2 in the tumor microenvironment of OSCC (Fig. 1L).

Wang et al. have found that CAV2 plays a vital role in facilitating invasion and increasing metastasis in HNSCC [12]. Meanwhile, our previous study has revealed an adverse association between CAV2 and E-cadherin expression in potentially malignant oral disorders and OSCC tissues. However, Wang et al. have reported that suppressing CAV2 in HNSCC cells had no impact on the protein level of E-cadherin. These discrepancies might be due to differences in experimental methodology and subjects. Although CAV2 has shown great potential in the apoptotic role, it has been poorly studied in OSCC. The current work revealed that the suppression of *CAV2* hindered the growth of OSCC cells and facilitated apoptosis. The MAPK signaling pathway includes ERK, JUN, and p38. MAPK pathways are an essential growth regulator that controls cell proliferation, apoptosis, and differentiation [47]. In the current investigation, analysis showed the enrichment of apoptosis and MAPK signaling pathways. The current study revealed higher levels of c-JUN and lower levels of p44/42 MAPK (Erk1/2), which suggested that *CAV2* knockdown might lead to the inhibition of the MAPK pathway. The increase of c-JUN might result from MAPK pathway changes, further promoting the expression of apoptosis-related genes. JUN modulates the balance between apoptosis, autophagy, and mitophagy by phosphorylating specific BCL2 protein family members, such as BCL2 [48]. Further findings showed that decreasing CAV2 in OSCC decreased BCL2 expression and increased c-JUN, suggesting that JUN activation may promote apoptosis by negatively regulating BCL2. CAS9 initiates the apoptotic pathway and

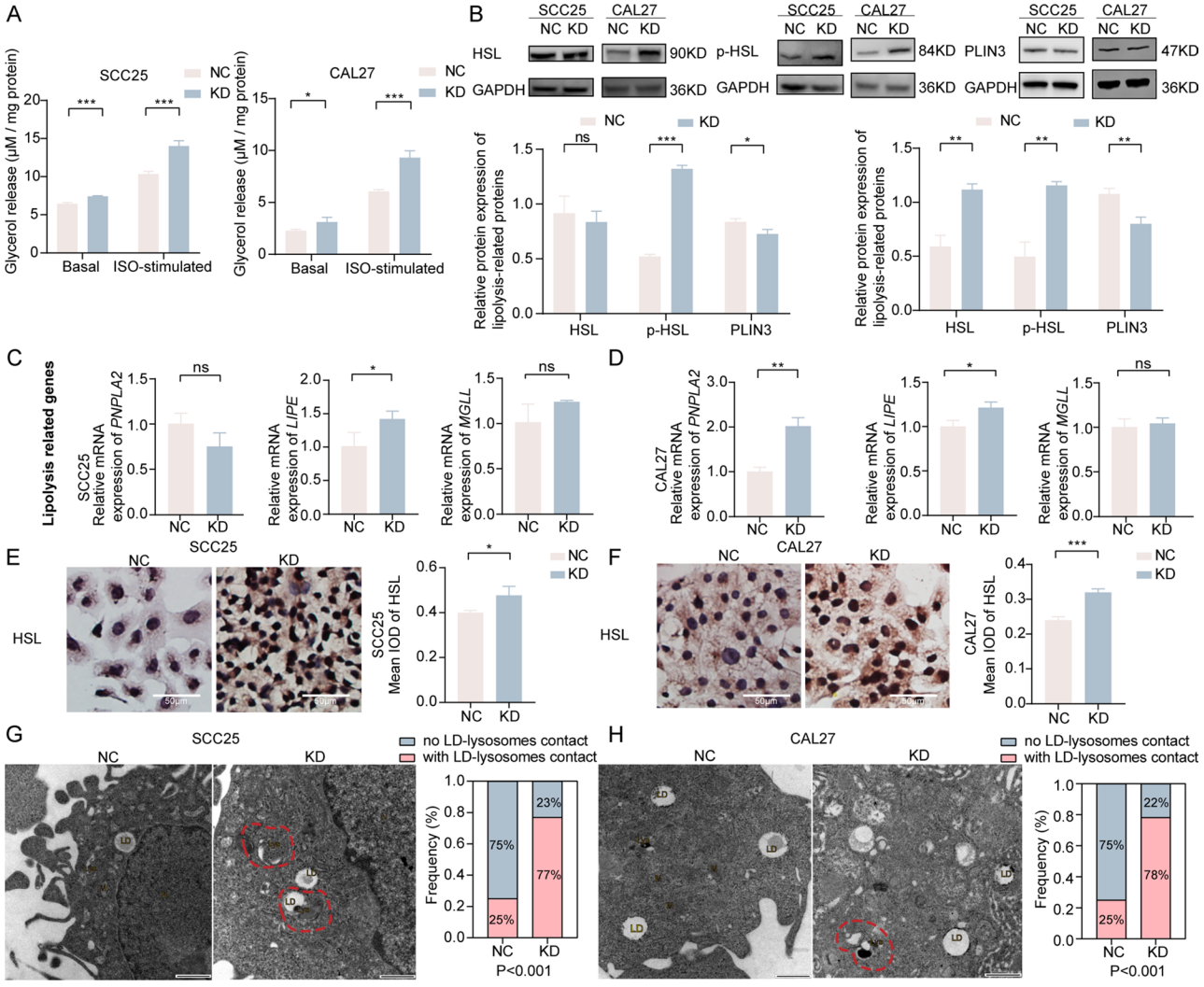

Fig. 6 Knockdown of *CAV2* promoted lipolysis in OSCC. (**A**) Basal and isoproterenol-stimulated lipolysis were measured in the conditional medium of SCC25 and CAL27 cells with *CAV2* knockdown. KD: shRNA targeting *CAV2*, labeled with GFP for green fluorescence tracking) or negative control, NC: scrambled control shRNA, labeled with GFP for green fluorescence tracking). (**B**) The protein expression levels of HSL, p-HSL, and PLIN3 in SCC25 and CAL27 cells after *CAV2* knockdown. Quantitative analysis of HSL, p-HSL, and PLIN3 protein expression in both KD and NC groups. (**C** and **D**) The *PNPLA2*, *LIPE*, and *MGLL* mRNA expression in SCC25 and CAL27 cells in OSCC cells after *CAV2* knockdown. (**E** and **F**) The HSL protein expression in SCC25 and CAL27 cells in OSCC cells after CAV2 knockdown. Scale bars = 50 μm. (**G** and **H**) Representative TEM of SCC25 and CAL27 cells with stable KD or NC. Scale bars = 1 μm. Frequency analysis of LD-lysosome contacts in SCC25 expressed NC (n=37) or KD (n=30) cells and CAL27 expressed NC (n=32) or KD (n=23) cells. All data were expressed as the mean ± SD (n≥3). Significance was determined by the Student's t-test (A-F) and the Chi-square test (**G** and **H**). *P<0.05, **P<0.01, ***P<0.001, ns = no significance. *CAV2*: Caveolin2; OSCC: oral squamous cell carcinoma; KD: shRNA targeting CAV2, labeled with GFP for green fluorescence tracking; NC: scrambled control shRNA, labeled with GFP for green fluorescence tracking; HSL: Hormone-sensitive lipase; PLIN3: Perilipin3; TEM: transmission electron microscope

activates CAS3, which is directly involved in cell death, including the disassembly of the cytoskeleton and the decomposition of DNA [49]. In this study, the analysis revealed higher levels of CAS9 and CAS3 protein in the *CAV2* knockdown group compared to the control group, which indicated that the intracellular apoptotic execution pathway was activated. While our findings provided initial evidence suggesting the involvement of MAPK signaling, additional investigations, such as gain- or loss-of-function studies, are needed to confirm this relationship and further elucidate the underlying mechanisms.

Previously, little was discovered of a possible mechanism of lipid metabolism mediated by CAV2. CAV2 was initially detected at the OSCC LDs in this research. A prior investigation found that the HepG2 cell line, a type of liver cancer cell, exhibited a deficiency of caveolins and had prominent LDs in culture [7]. In contrast, this study showed that overexpression and knockdown of *CAV2*

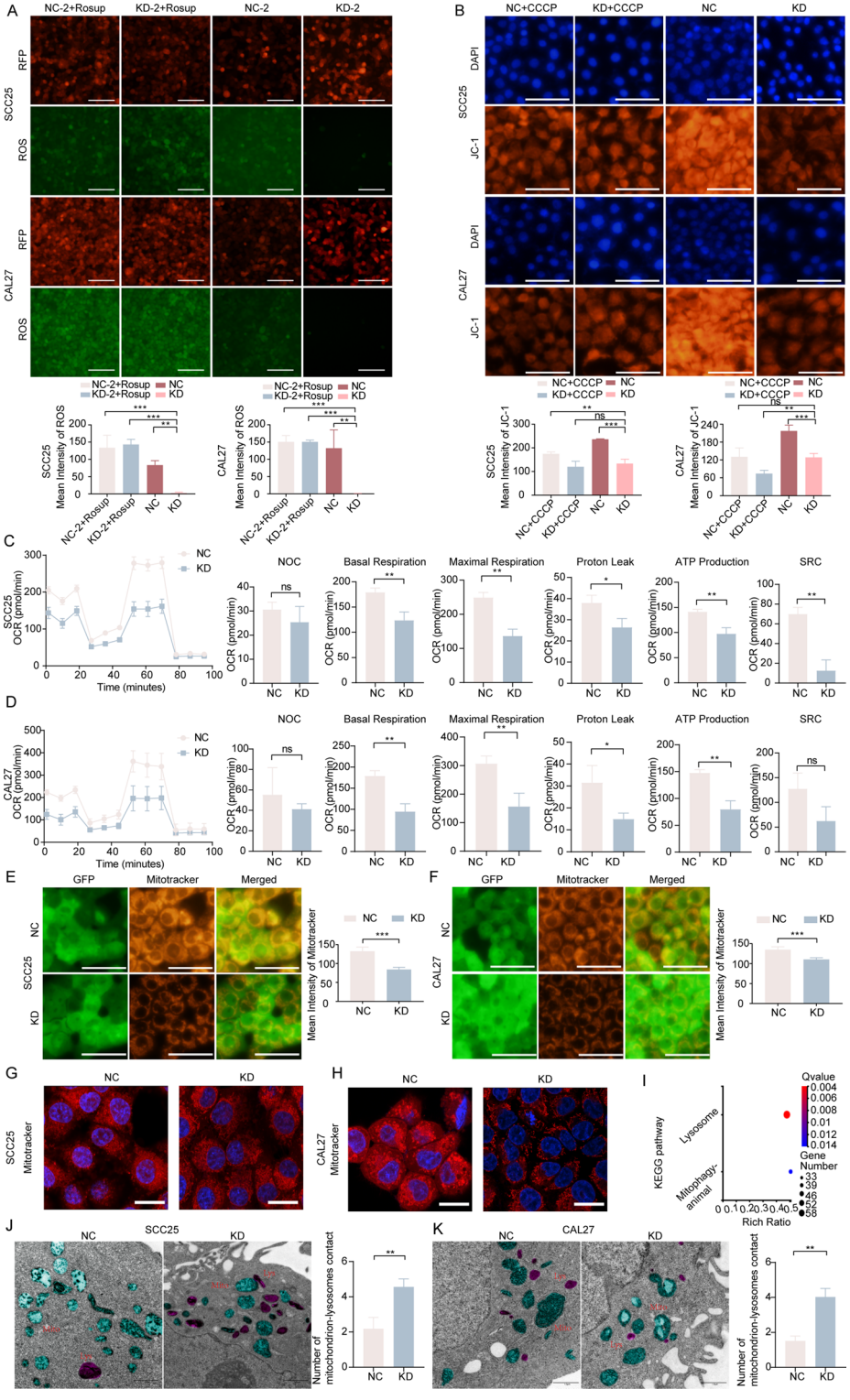

Fig. 7 (See legend on next page.)

revealed a striking change in LD dynamics in OSCC cells. Specifically, when the *CAV2* was overexpressed, LDs were smaller and more numerous, whereas, with *CAV2* knockdown, LDs were fewer and more prominent. The modulation of *CAV2* expression demonstrated significant effects on the characteristics of LDs, likely due to several reasons. Firstly, the propensity for smaller and more numerous LDs with *CAV2* overexpression implied

(See figure on previous page.)

Fig. 7 Knockdown of *CAV2* induced mitochondrial dysfunction in OSCC. (**A**) Measurement of ROS in CAL27 and SCC25 cells treated with *CAV2* knockdown (KD-2) or negative control (NC-2). ROS levels were quantified using the DCFH-DA probe and observed under a fluorescence microscope. Cells expressed RFP (red), and ROS were labeled with DCFH-DA (green). Scale bars = 100 μm. Five visual fields per sample were randomly selected for statistical analysis. (**B**) Assessment of MMP in CAL27 and SCC25 cells treated with KD or NC using the JC-1 probe. Nuclei were stained with DAPI (blue), and MMP was visualized with JC-1 (red). The quantitative analysis of MMP was performed. Scale bars = 50 μm. (**C** and **D**) Seahorse analysis of mitochondrial respiration in CAL27 and SCC25 cells treated with KD or NC was conducted. Non-mitochondrial oxygen consumption showed no significant difference between the KD and NC groups. Results showed that KD significantly decreased basal respiration, maximal respiration, proton leak, and ATP production in both cell lines compared to NC. Spare respiratory capacity analysis revealed a significant reduction in SCC25 cells, whereas no significant change was observed in CAL27 cells. (**E** and **F**) Mitochondrial intensity in OSCC cells (CAL27 and SCC25) treated with NC or KD was measured using the Mitotracker probe. GFP (green) labeled cells and mitochondria were stained with Mitotracker (red). Scale bars = 50 μm. Quantitative analysis was based on five random fields per sample. (**G** and **H**) Mitochondrial morphology was assessed in OSCC cells using Mitotracker staining. In the control group (NC), mitochondria appeared disc-shaped, whereas in the *CAV2* knockdown group (KD), mitochondria were elongated and fragmented. Scale bars = 10 μm. (**I**) KEGG pathway enrichment analysis based on RNA sequencing data identified lysosome- and mitophagy-related pathways as significantly enriched in KD cells compared to NC cells. (**J** and **K**) TEM images of CAL27 and SCC25 cells showed increased interactions between mitochondria and lysosomes in KD cells compared to NC cells, highlighting enhanced mitophagy. Pseudocolors were applied to distinguish mitochondria (blue) and lysosomes (purple-red). Scale bars = 1 μm. The frequency of mitochondria-lysosome contacts was quantified and compared between groups (NC: n=32; KD: n=31). All data were expressed as the mean ± SD ($n \geq 3$) without special instructions. The one-way **A**NOV**A** determined significance with Dunn's multiple comparison tests (**A** and **B**) and the Student's t-test (**C**-**F**, **J**, and **K**). *P<0.05, **P<0.01, ***P<0.001, ns = no significance. *CAV2*: *CAVEOLIN2*; KD: shRNA targeting *CAV2*, labeled with GFP for green fluorescence tracking) or negative control, NC: scrambled control shRNA, labeled with GFP for green fluorescence tracking). KD-2: shRNA targeting CAV2, labeled with RFP for red fluorescence tracking; NC-2: scrambled control shRNA, labeled with RFP for red fluorescence tracking. OSCC: oral squamous cell carcinoma; ROS: reactive oxygen species; DCFH-DA: 2',7'-dichlorodihydrofluorescein diacetate; DAPI: 4',6-diamidino-2-phenylindole; MMP, mitochondrial membrane potential; TEM: transmission electron microscope; Mito: mitochondria; Lys: lysosomes

a role in LD formation and stability, which indicated that CAV2 might facilitate the biogenesis of LDs or contribute to their structural integrity. Conversely, *CAV2* knockdown appeared to disrupt these processes. Secondly, caveolins play a critical role in the internalization of lipid molecules in cells. Tumor cells primarily utilize endocytosis to uptake nutrients. A down-regulation of FA absorption might have caused decreased LDs elicited by *CAV2* knockdown. Thirdly, the breakdown of LDs might be caused by the activation of lipolysis following *CAV2* knockdown. In summary, the alterations in LD characteristics might indicate broader shifts in cellular metabolic states.

Therefore, the current study thoroughly examined the lipid composition in OSCC cells using lipidomics following the suppression of *CAV2*. The elevated DG and FAs caught our attention. DG is an essential intermediate metabolite that plays a crucial role in cell signaling, lipid metabolism, and energy. Sources of DG include hydrolysis of triglyceride, intermediates in lipid synthesis, degradation of cell membranes, and signal transduction during metabolic regulation [50]. Among the top 20 most relevant terms related to lipid metabolism include lipolysis, linoleic acid metabolism, and biosynthesis of unsaturated FAs, which were significantly enriched. Since DG and FA are direct lipolysis products, their accumulation implied an active breakdown of triglycerides (TGs). Therefore, we focused subsequent research on whether the increase in DG and FA was partially derived from lipolysis.

Glycerol release increases during lipolysis [51]. Our data indicated that knocking down *CAV2* in OSCC cells increased glycerol levels in the culture supernatant. Increased lipolysis activates the lipolysis-related genes *PNPLA2*, *LIPE*, and *MGLL* in adipose tissue [52]. The mRNA expression of lipolysis-related genes *LIPE* was elevated in the *CAV2* knockdown group compared to the corresponding control group. PLIN3 interacts with lipases on the surface of LDs, which can inhibit lipase activity, thereby limiting the progression of lipolysis in LDs [47]. Our findings demonstrated that silencing *CAV2* resulted in a decreased expression of PLIN3 compared to the control group. Furthermore, increased total HSL protein levels and phosphorylation were detected in OSCC cells following *CAV2* knockdown, indicating enhanced HSL activity. This finding aligned with the observed lipid profile changes, which implied that *CAV2* knockdown promoted lipolysis. However, we did not identify specific regulatory proteins involved in this process, limiting our understanding of the complete regulatory network underlying this lipolytic mechanism. Therefore, future research should focus on applying proteomics techniques to identify and validate these potential regulators. Contact between LDs and lysosomes usually means that substances on the LDs may be directed to lysosomes for degradation [53]. In our study, TEM showed lysosomes were recruited to LDs, which verified the enhanced lipolysis. During lipolysis, we usually expect to see a decrease in TGs and an increase in FAs. Following the knockdown of *CAV2* in SCC25 cells, there was no significant change in monoglycerol and TG based on the current detection method (Fig. H–S5I). This discrepancy might be indicative of partial lipolysis. Moreover, while cholesterol esters are hydrolyzed into free cholesterol during LD lipolysis, the knockdown of *CAV2* did not produce notable alterations in total cholesterol levels in OSCC cells (Fig. J), probably owing to compensatory mechanisms or cholesterol redistribution that preserve overall cholesterol homeostasis despite localized hydrolytic activity.

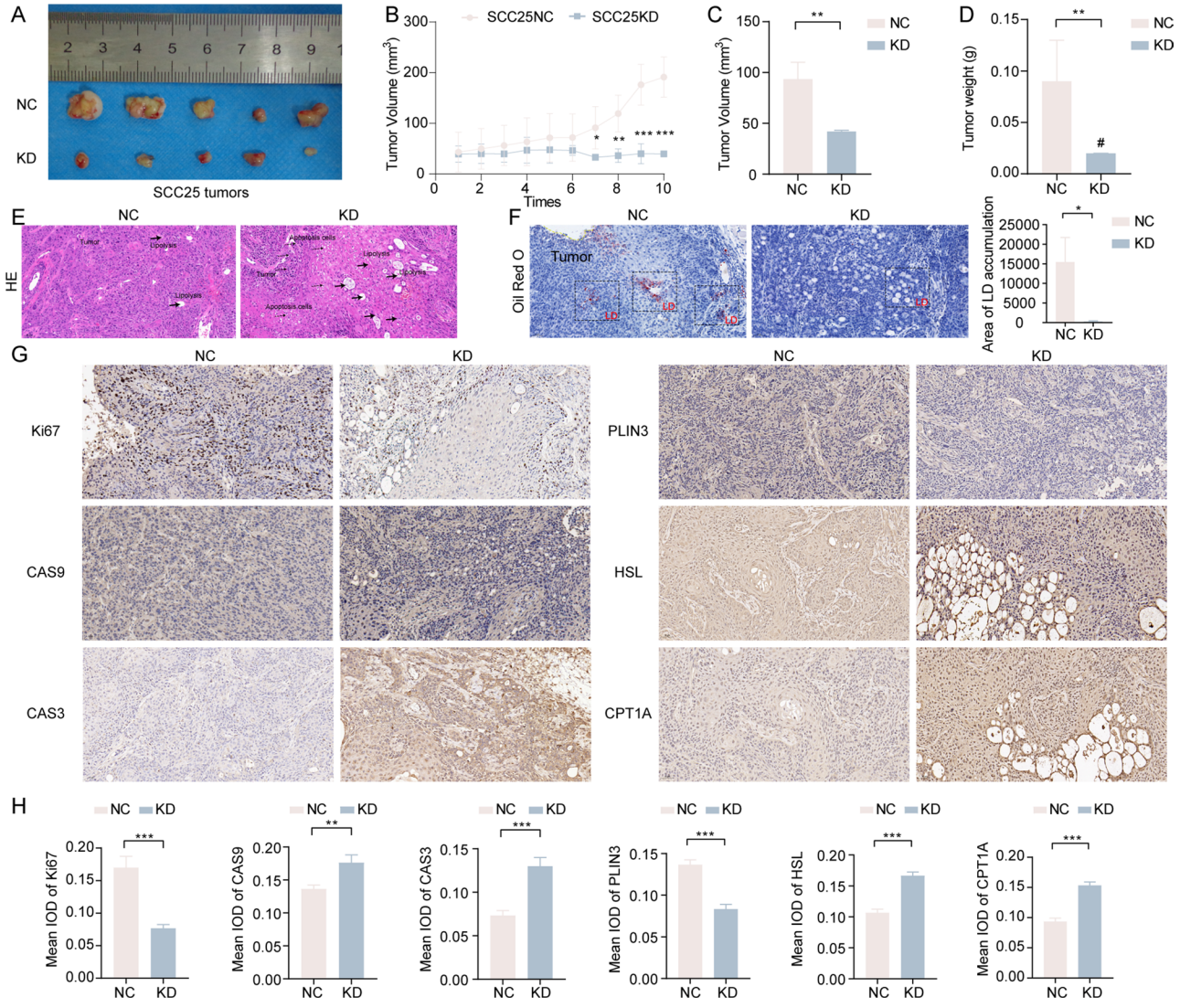

Fig. 8 Knockdown of *CAV2* inhibited OSCC progression in vivo. (**A**) Xenograft tumors of SCC25 cells with knockdown (KD: shRNA targeting *CAV2*, labeled with GFP for green fluorescence tracking) or negative control (NC: scrambled control shRNA, labeled with GFP for green fluorescence tracking) groups (n = 5 per group). (**B**) Tumor growth curves for SCC25 NC cells and SCC25 KD cells subcutaneously transplanted into nude mice. (**C**) Tumor volumes of NC and KD groups. (**D**) Tumor weight of NC and KD groups. (**E**) Representative HE images of tumors in NC and KD groups. Scale bars = 50 μm. (**F**) Representative Oil Red O staining images of tumors in NC and KD groups. Scale bars = 50 μm. Quantitative analysis of Oil Red O staining area was performed using Image-Pro Plus (IPP) software. (**G**) Representative IHC images of Ki67, CAS9, CAS3, PLIN3, HSL, and CPT1A in NC and KD groups in xenograft tumors. (**H**) Mean IOD analysis of Ki67, CAS9, CAS3, PLIN3, HSL, and CPT1A in NC and KD groups in xenograft tumors. Scale bars = 50 μm. *P<0.05, **P<0.01, ***P<0.001, ns = no significance. Normally distributed variables were presented as mean ± SD (n≥3), while non-normally distributed data were presented as median ± IQR and labeled by '#'. Significance was determined by the Student's t-test (A-C, F, G, and H), Mann-Whitney U (**D**). KD: knockdown; NC: negative control; HE: hematoxylin and eosin; OSCC: oral squamous cell carcinoma; *CAV2*: *CAVEOLIN2*; KD: shRNA targeting *CAV2*, labeled with GFP for green fluorescence tracking; NC: scrambled control shRNA, labeled with GFP for green fluorescence tracking; IF: immunofluorescence staining; DAPI: 4',6-diamidino-2-phenylindole; IHC: immunohistochemical staining; CAS9: Caspase9; CAS3: Caspase3 PLIN3: Perilipin3; HSL: Hormone-sensitive lipase; CPT1A: Carnitine O-palmitoyltransferase 1 A; IOD: integrated optical density; IQR: interquartile range

Moreover, despite the indirect evidence for lipophagy in this study, it was suggested that the connections between lipids and lysosomes and autophagy-related pathways required additional examination.

Notably, intracellular lipolysis can promote tumor progression by fueling cell growth. Our study found that knocking down *CAV2* in OSCC enhanced lipolysis while inhibiting tumor growth. The type of FAs produced after *CAV2* knockdown might play an important role. Research suggests that saturated and monounsaturated FAs promote tumor growth [54], whereas PUFAs have anticancer potential in cancers [55]. Therefore, it is essential to consider the potential sources of these PUFAs in the context of our findings. First, *CAV2* silencing might

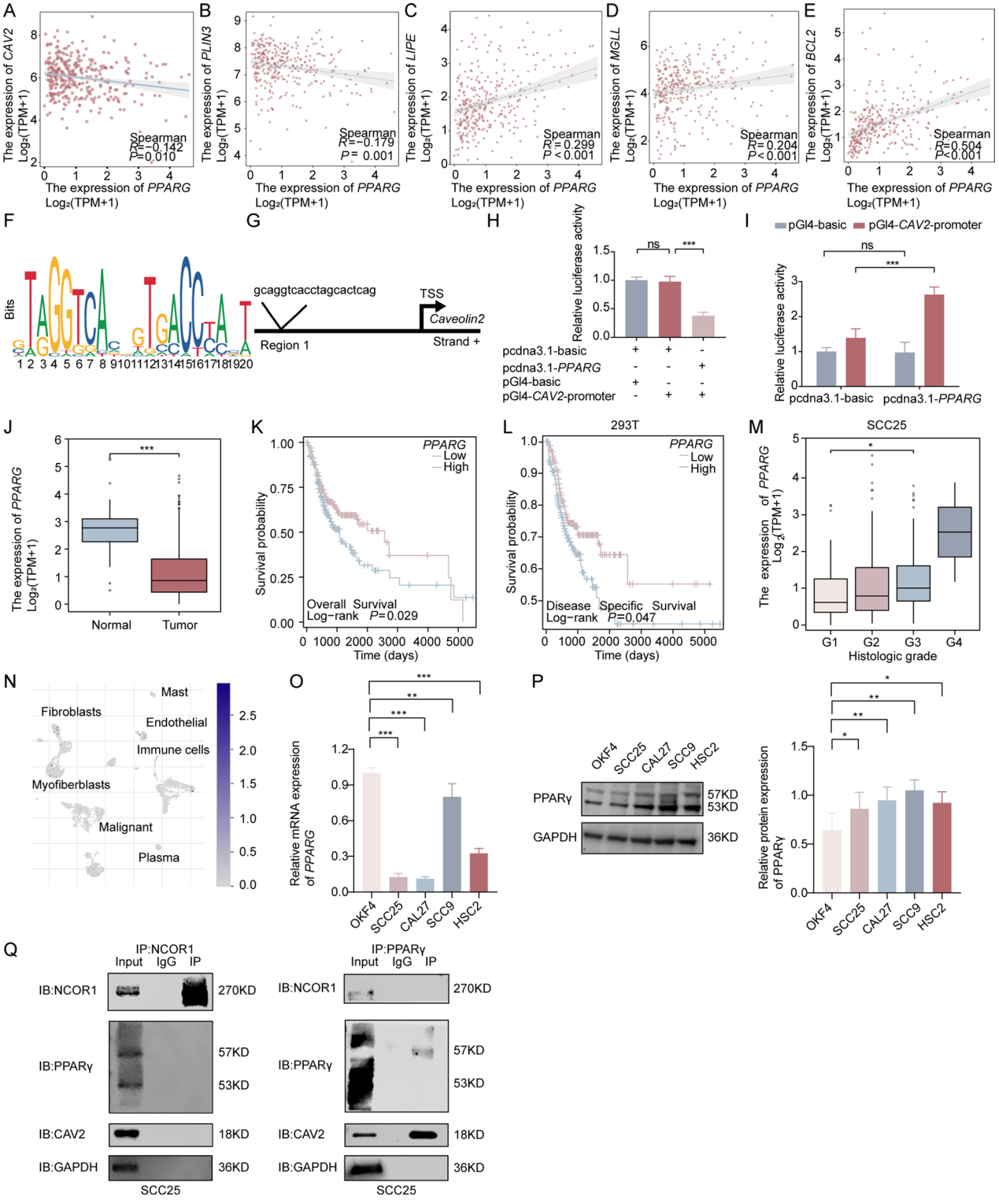

Fig. 9 (See legend on next page.)

alter the lipid composition, leading to the release of more PUFAs. In the present study, the other lipid composition of OSCC cells was changed, involving glycerolipids, glycerophospholipids, sphingolipids, and saccharolipids. Second, FA esterification may also be disrupted after *CAV2* knockdown in OSCC, but this still requires further experimental validation. FA esterification refers to the biochemical process of mixing free FAs with an

(See figure on previous page.)

Fig. 9 Dysregulated transcriptional repression of CAV2 by PPARγ in OSCC. (**A**-**E**) Correlation analysis of the *PPARG* between *CAV2*, *PLIN3*, *LIPE*, *MGLL*, and *BCL2* from TCGA. (**F**) Illustration of the PPARγ motif (MA0065.1). (**G**) Predicted binding regions for PPARγ on the promotor of *CAV2* using the FIMO database. (**H**) Dual luciferase assay using HEK293T cells after transfection with the indicated plasmids (RL-TK, pGL4-Basic, pGL4-*CAV2*-promoter reporter, pcdna3.1-basic, and human pcdna3.1-*PPARG*). (**I**) Dual luciferase assay using SCC25 cells after transfection with the indicated plasmids (RL-TK, pGL4-Basic, pGL4-*CAV2*-promoter reporter, pcdna3.1-basic, and human pcdna3.1-*PPARG*). (**J**) The expression of *PPARG* in OSCC (n=330) and normal samples (n=32) was acquired from TCGA. (**K**) Overall survival rates according to *PPARG* expression in OSCC. (**L**) Disease-specific survival rates according to *PPARG* expression in OSCC. (**M**) *PPARG* expression in OSCC of different histologic grades. n=322. (**N**) Distribution of *PPARG* in different cells in HNSC_GSE103322 datasets. (**O**) Relative mRNA expression of *PPARG* in different cell lines. (**P**) Protein expression of PPARγ in different cell lines, with quantitative analysis of WB results. (**Q**) Reciprocal Co-IP followed by WB showing pull down of NCOR1 and PPARγ using antibodies against each versus IgG control pull down in SCC25 cells. Pull-down samples were analyzed for NCOR1, PPARγ, and CAV2. Data were overlaid by the median and IQR (**J** and **M**). Data were presented as cumulative survival curves (**K** and **L**). Data were represented as mean ± SD of three independent experiments (**H**, **I**, **O**, and **P**). Correlation analysis was performed using Spearman's correlation (**A**-**E**). Significance was determined by one-way ANOVA (**H**, **I**, **O**, and **P**), the Wilcoxon rank sum test (**J**), the log-rank test (**K** and **L**), and the Kruskal-Wallis test with Dunn's multiple comparison tests (**M**). *$P < 0.05$, **$P < 0.01$, ***$P < 0.001$, ns: no significance. IQR: interquartile range; *CAV2*: *CAVEOLIN2*; *PLIN3*: *PERILIPIN3*; OSCC: oral squamous cell carcinoma; PPARγ: peroxisome proliferator-activated receptor gamma. TCGA: The Cancer Genome Atlas; Co-IP: co-immunoprecipitation; WB: western blot

alcohol, typically glycerol, to form ester compounds [56]. This process is crucial in the initial stages of lipid synthesis, primarily for producing TG, the main form of stored energy in animals. In our study, an increase in FA was observed following the knockdown of *CAV2*, suggesting disturbed FA esterification. From another perspective, phospholipid hydrolysis is critical in cell signaling and membrane dynamics. Hydrolysis involves the catalytic action of specific enzymes, such as phospholipases, which break down phospholipids to produce PA, DG, and FAs. In the study, an increase in PA, DG, and FA was observed after *CAV2* knockdown in OSCC, supporting the central role of phospholipid hydrolysis in cellular metabolism and signaling. Therefore, *CAV2*-mediated phospholipid hydrolysis is also worth exploring. The specific source of PUFAs needs to be traced using radioactive labeling experiments.

To identify the source of PUFAs, a combined analysis of lipidomics and RNAseq was conducted to search for key genes regulating PUFAs after *CAV2* knockdown. Genes may encode enzymes, transporters, or regulators that affect lipid metabolism. Our study revealed that among the top 20 highly correlated gene-lipid pairs, lipids in 19 pairs were enriched in PUFAs, further demonstrating the critical role of PUFAs in the lipid regulatory network following *CAV2* knockdown. For instance, FA 24:6 was found to be positively correlated with GSTM4 in this study. Being a member of the glutathione S-transferase (GST) family, GSTM4 primarily catalyzes the binding interaction between glutathione and electron affinity molecules, which is involved in intracellular detoxification and metabolic processes. GST enzymes defend cells against chemical toxicity and oxidative damage [57]. The role of GSTM4 in protecting against oxidative stress may affect the oxidative status of lipids, including FA 24:6. Long-chain PUFAs are susceptible to oxidation, and the GST enzyme may help protect these lipids from damage. The antioxidant effect of GSTM4 may affect intracellular signaling pathways, thereby indirectly affecting the metabolism of FA 24:6. Moreover, the association of differential genes with differential PUFAs illustrated a vast regulatory landscape, highlighting a diversified biological impact on the metabolism of PUFAs mediated by CAV2, which provided targets for therapeutic intervention in the future.

In addition to delineating the origins of PUFAs after the downregulation of *CAV2* in OSCC cells, our study also explored their potential destinations within cellular metabolic pathways. CPT1A is a crucial transport protein that plays a key role before FAs enter the mitochondria [35]. The study presented analyses demonstrating the potential connection between PUFAs and the CPT1A protein. Additionally, the present study found elevated CPT1A protein expression levels after knocking down *CAV2* in OSCC cells. In the current research, genes involved in mitochondrial function and structure were differentially expressed after interfering with *CAV2* in OSCC cells, which suggested that PUFA deposition induced by CAV2 might affect the function of mitochondria. Herein, we hypothesized that the accumulation of PUFAs resulting from *CAV2* knockdown was likely directed toward the mitochondria. Since we have not yet completed the metabolic flux analysis, we conducted explorations using molecular dynamics analyses instead. It was found that the four major accumulated PUFAs exhibited binding affinity to CPT1A, suggesting that they were likely directed to the mitochondria.

Linoleic acid (LA) is one of the essential components of mitochondrial membrane phospholipids. The phospholipid composition of the mitochondrial membrane directly affects its fluidity and function, and the LA content affects these properties [58]. The current research demonstrated a combined study of the transcriptome and lipidome, specifically focused on the metabolic pathways associated with LA metabolism (Fig. 5D), which suggested that the knockdown of *CAV2* in OSCC might result in the dysregulation of mitochondrial function. Our investigation illustrated that the knockdown of *CAV2* resulted in decreased ROS levels, a discernible alteration in MMP and mitochondria mass, impaired

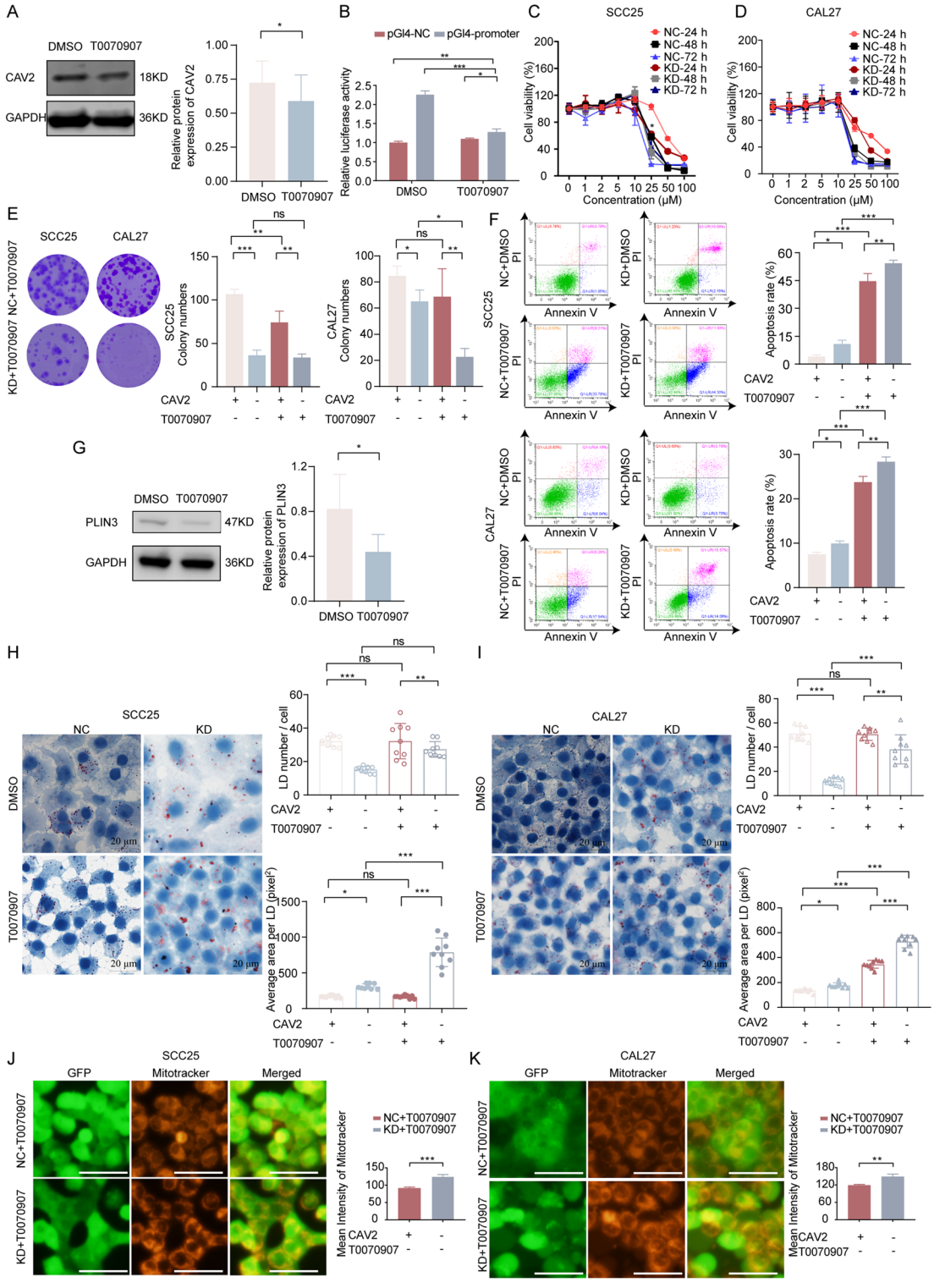

Fig. 10 (See legend on next page.)

mitochondria respiration, and reduced intensity of mitochondrial staining, suggesting that downregulating *CAV2* led to mitochondrial dysfunction in OSCC cells. Mitophagy is activated as a quality control mechanism when mitochondrial function is impaired or mitochondria are damaged [59]. In the current research, enhanced mitophagy was observed by TEM and transcriptome analysis. In our study, other PUFAs, such as lipids FA (20:5), were

(See figure on previous page.)

Fig. 10 Enhanced suppression of CAV2 using transcriptional repression by T0070907 promoted cell apoptosis, lipolysis, and mitochondrial dysfunction in OSCC. (**A**) CAV2 protein in SCC25 cells treated with T0070907 (25 μM, 48 h). Quantitative analysis of CAV2 protein expression was performed. (**B**) After treatment for SCC25 cells with T0070907 (25 μM, 48 h), dual luciferase assay using SCC25 cells after transfection with the indicated plasmids (RL-TK, pGL4-basic, pGL4-*CAV2*-promoter reporter). (**C** and **D**) Cell viability assay showing IC_{50} values of T0070907 (0, 1, 2, 5, 10, 25, 50, 100 μM) in OSCC cell lines expressing shRNA targeting *CAV2* (KD) and scrambled control shRNA (NC) after culturing for 24 h, 48 h, and 72 h. Both KD and NC cells were labeled with GFP for green fluorescence tracking. (**E**) Colony formation assay in SCC25 and CAL27 cells expressing KD or NC, followed by treatment with T0070907 (25 μM, 48 h). Colonies were quantified after 7 days of treatment followed by 5 days of culture. The quantitative analysis compares T0070907-treated groups to untreated KD and NC groups. (**F**) Flow cytometry analysis of apoptosis in SCC25 and CAL27 cells expressing KD or NC, treated with T0070907 (25 μM, 48 h) or DMSO (control), using APC Annexin V/PI apoptosis detection. Quantitative apoptosis rate analysis was provided. (**G**) PLIN3 protein in SCC25 cells treated with T0070907 (25 μM, 48 h). Quantitative analysis of PLIN3 protein expression was performed. (**H** and **I**) Oil Red O staining of NC and KD OSCC cells treated with T0070907 (25 μM) for 48 h. Quantitative analysis of LD number per cell and average area per LD in OSCC cells. Scale bars = 20 μm. Seven visual fields per sample were randomly selected for statistical analysis. (**J** and **K**) The Mitotracker probe was used to measure the changes in mitochondrial staining intensity in the OSCC cell lines comprising CAL27 and SCC25 cells treated with shCAV2 or vehicle control treated with T0070907 (25 μM, 48 h) by the fluorescence microscope. Cells were labeled with GFP (green), and mitochondria were labeled with Mitotraker (red). Scale bars = 50 μm. Five visual fields per sample were randomly selected for statistical analysis. Normally distributed variables are presented as mean ± SD ($n \geq 3$). Significance was determined by Student's t-test (A, G, J, and K), one-way ANOVA with Turkey's multiple comparison tests (B, E, F, H, and I), and two-way ANOVA with Bonferroni post-test (**C** and **D**). $^{*}P < 0.05$, $^{**}P < 0.01$, $^{***}P < 0.001$, ns: no significance. CAV2: Caveolin2; OSCC: oral squamous cell carcinoma; KD: shRNA targeting *CAV2*, labeled with GFP for green fluorescence tracking; NC: scrambled control shRNA, labeled with GFP for green fluorescence tracking; PLIN3: Perilipin3; PPARγ: peroxisome proliferator-activated receptor gamma; DMSO: dimethyl sulfoxide; IQR: interquartile range

enriched by lipomics, referred to as eicosapentaenoic acid, an omega-3 series PUFA. Omega-3 series PUFAs cause cancer cell apoptosis by affecting cell signaling pathways, increasing oxidative stress, regulating gene expression, and activating apoptotic pathways [60, 61]. Our team has summarized that Omega-3 helps prevent oral cancer [62]. Therefore, it is worth exploring whether the accumulation of PUFAs caused by *CAV2* knockdown contributes to the increased apoptosis observed in our experiments.

The mouse xenograft model we used investigated the role of CAV2 in OSCC tumorigenicity and provided insights into the connection between CAV2 expression and tumor growth. Cells with *CAV2* knockdown exhibited a noticeable impairment in their ability to produce tumors, as seen by a reduction in tumor size and mass compared to the control group. The HE-stained sections of tumor tissues showed increased lipolysis and apoptosis, consistent with the observations made at the cellular level.

The involvement of PPARγ in malignancies is still a subject of debate and could vary depending on the specific type and stage of cancer. Activation of PPARγ inhibits the progression of the majority of cancer types. The activity and function of PPARγ are regulated mainly by its post-translational modifications, which affect its binding to DNA, interaction with cofactors, and degradation and stability [63]. The increased expression of PPARγ protein is associated with the spread of cancer and poor clinical results in HNSCC, suggesting that PPARγ functions as an oncogene in HNSCC [21]. Contrarily, our research revealed that the expression of *PPARG* mRNA was decreased in individuals with OSCC compared to those without the condition. Consistently, qRT-PCR analysis showed reduced expression of *PPARG* in OSCC cells relative to the normal human oral epithelial cells. WB analysis revealed that the expression of PPARγ was elevated in OSCC cells compared to OKF4 cells. The study identified a discrepancy between reduced *PPARG* mRNA and elevated PPARγ protein levels in OSCC cells. This discrepancy may result from post-transcriptional and post-translational regulatory mechanisms, such as post-translational modifications (e.g., phosphorylation, ubiquitination) that stabilize PPARγ protein despite lower mRNA levels. Cancer stage, microenvironment, and cofactor interactions could differentially regulate PPARγ activity, explaining its dual roles as a tumor suppressor and oncogene in varying contexts.

Prior research has seldom investigated the interplay between CAV2 and PPARγ. The potential binding site between PPARγ and CAV2 was identified using bioinformatics methods, and the PPI network revealed their interaction in this research. Furthermore, dual-luciferase reporter assays have confirmed that overexpression of PPARγ can inhibit CAV2 activity in 293T cells, suggesting that PPARγ suppressed gene expression by acting through transcriptional repressors. The PPARγ/NCOR1 complex has demonstrated its regulatory potential in cancer [23]. Notably, overexpression of PPARγ elevated CAV2 activity in SCC25 cells, suggesting that PPARγ might enhance CAV2 transcription through a mechanism that does not involve forming a complex with NCOR1, leading to a different regulatory effect than 293T cells. In the present study, CAV2 was coimmunoprecipitated with PPARγ from SCC25 cell lysates, confirming that PPARγ and CAV2 coexisted in a complex. Moreover, in OSCC cells, PPARγ/CAV2 complex could not recruit the corepressor NCOR1, as evidenced by Co-IP experiments, indicating that the transrepression mechanism of PPARγ on CAV2 was dysregulated in OSCC. Subsequently, we utilized an inverse agonist known to facilitate the formation of the PPARγ/NCOR1 complex, which significantly inhibited the activity of the CAV2 promoter, further supporting this hypothesis.

PPAR-signaling inverse agonists have received limited attention. The present study visualized the specific binding of T0070907 to the Arg 288, Cys 285, and Met 348 amino acids via pi-H, H donor, and H donor of the PPARγ receptor. Kojetin et al. have shown the significance of a water-mediated hydrogen bond network that connects the T0070907 pyridyl group to Arg288, which is accomplished through X-ray crystallography, molecular dynamics simulations, and mutagenesis, along with activity testing [64]. Therefore, using T0070907 to reverse the dysregulation transcriptional repression of PPARγ to inhibit *CAV2* gene expression in OSCC was feasible. In the present research, T0070907 combined *CAV2* knockdown treatment significantly inhibited OSCC proliferation and colony growth, triggered massive cell apoptosis, promoted lipolysis, altered LD dynamics, and led to mitochondrial dysfunction in vitro.

Conclusion

In this study, our research explored the essential role of CAV2 in OSCC, elucidating its critical involvement in processes such as apoptosis, lipolysis, and mitochondrial dysfunction. Upregulation of *CAV2* expression was strongly associated with poor prognosis of OSCC patients. In contrast, reduction of its expression effectively inhibited the growth of OSCC, demonstrating the potential of CAV2 as a therapeutic target. Furthermore, the inhibition of *CAV2* resulted in the accumulation of DG and PUFAs, elevated apoptosis and lipolysis, and triggered mitochondrial dysfunction, offering several potential intervention points for OSCC therapies. Our study also highlighted the dysregulation of CAV2 transcription by PPARγ in OSCC. The effectiveness of the PPARγ inverse agonist T0070907 demonstrated the potential of targeted therapy in OSCC. These findings confirmed the essentiality of CAV2 as a crucial therapeutic objective for OSCC and emphasized the significance of concurrently investigating multiple therapeutic approaches to attain successful treatment.

Abbreviations

CAV2	Caveolin2
OSCC	Oral squamous cell carcinoma
LDs	Lipid droplets
PLIN	Perilipin
PUFAs	Polyunsaturated fatty acids
ROS	Reactive oxygen species
MMP	Mitochondrial membrane potential
FAs	Fatty acids
PPARγ	Peroxisome proliferator-activated receptor γ
Co-IP	Coimmunoprecipitation
PCA	Principal component analysis
OPLS-DA	Orthogonal partial least squares discriminant analysis
rCCA	Canonical correlation analysis
TEM	Transmission electron microscopy
CPT1A	Carnitine palmitoyltransferase 1
PC	Phosphatidylcholine
PE	Phosphatidylethanolamine
PI	Phosphatidylinositol
OAHFA	(O-acyl)-1-hydroxy fatty acid
SM	Sphingomyelin
PG	Phosphatidylglycerol
MGDG	Monogalactosyldiacylglycerol
LPC	Lysophosphatidylcholine
PS	Phosphatidylserine
PA	Phosphatidic acid
DG	Diglyceride
LA	Linoleic acid

Supplementary Information

The online version contains supplementary material available at https://doi.org/10.1186/s13578-025-01399-6.

Supplementary Material 1

Supplementary Material 2

Supplementary Material 3: S1 (A) Transfection efficiencies of SCC25 and CAL27 cells transfected with shCAV2-1 (KD) and shControl-1 (NC) were assessed after puromycin selection. GFP fluorescence marked cells expressing shRNA. Scale bars = 100 μm. (B) Transfection efficiencies of SCC25 and CAL27 cells transfected with shCAV2-2 (KD-2) and shControl-2 (NC-2) were evaluated following puromycin selection. RFP fluorescence marked cells expressing shRNA. Scale bars = 100 μm.

Supplementary Material 4: S2. Analysis of the RNAseq of SCC25NC and SCC25KD. (A–C) Quality control and distribution of RNAseq data: Pearson correlation, TPM distribution, and PCA plot. (D) Volcano plot showing DEGs. (E) Heatmap depicting the expression of DEGs. N=3. ***CAV2***: ***Caveolin2***; TPM: transcripts per million; PCA: principal component analysis; DEGs: differentially expressed genes. KEGG: Kyoto Encyclopedia of Genes and Genomes; NC: scrambled control shRNA, labeled with GFP for green fluorescence tracking; KD: shRNA targeting ***CAV2***, labeled with GFP for green fluorescence tracking.

Supplementary Material 5: S3. Investigation of LDs in human oral keratinocyte cell line and OSCC cells at 24 h, 48 h, and 72 h. (A-C) Representative graphs of LDs of human oral keratinocyte cell line OKF4, OSCC cell line SCC25, and CAL27 cultured for 24 h, 48 h, and 72 h, respectively. Scale bars = 20 μm. (D-F) Quantifying LD numbers per cell in OKF4, SCC25, and CAL27 cells. (G-I) Quantification of LD area per cell in OKF4, SCC25, and CAL27 cells. (J-L) Comparison of LD numbers per cell in OKF4, SCC25, and CAL27 cells cultured for 24 h, 48 h, and 72 h, respectively. (M-O) Comparison of LD area per cell in OKF4, SCC25, and CAL27 cells cultured for 24 h, 48 h, and 72 h, respectively. (D, F-O) Data were represented as mean ± SD of three independent experiments. (E) Data were overlaid by the median and IQR. Seven visual fields per sample were randomly selected for statistical analysis under high magnification. The Welch ANOVA determined significance with Dunn's multiple comparison tests (D, H, and J-O), the Kruskal-Wallis test with Dunn's multiple comparison tests (E), and one-way ANOVA with a post-hoc Tukey's HSD test (F, G, and I). *P < 0.05, **P < 0.01, ***P < 0.001, ns: no significance. LDs: lipid droplets; OSCC: oral squamous cell carcinoma.

Supplementary Material 6: S4. Verification of CAV2 overexpression in OSCC cells after lentivirus infection. (A) The overexpression of ***CAV2*** in SCC25 and CAL27 cells after the RT-qPCR verified lentivirus infection. (B) The overexpression of CAV2 in SCC25 and CAL27 cells after the WB analysis verified lentivirus infection. Quantification of (B). (C) Quantification of CAV2 fluorescence intensity in CON and OE OSCC cell groups. (D) Quantifying LD number per nuclei based on BODIPY™ 493/503 staining in CAV2 OE and CON groups.(E) GO cellular component analysis showed significant enrichment of lipid droplets in CAV2-knockdown OSCC cells. Data were represented as mean ± SD of three independent experiments. For statistical analysis, three random high-magnification visual fields per sample were selected. Significance was determined by Student's t-test (A-D), ***P*** < 0.05, ****P*** < 0.01, *****P*** < 0.001. CAV2: Caveolin2; OSCC: oral squamous cell carcinoma; RT-qPCR: quantitative Real-time PCR; WB: Western Blot; OE: CAV2 overexpression using lentiviral-mediated overexpression (no fluorescence labeling); CON: control using lentiviral-mediated empty vector (no fluorescence labeling); LD: lipid droplet.

Supplementary Material 7: S5. Lipidomic analysis of SCC25NC and SCC25KD. (A) CV Distribution of Lipid Molecules. (B) Base peak intensity chromatograms for positive and negative ions. (C–E) Multivariate analysis: PCA score plot, OPLS-DA score plot, and response sequencing verification for OPLS-DA. (F) Volcano plot for differentially abundant lipids. (G) Lipid class distribution of detected lipids. (H) Detected changes in lipid sub-class. Levels of TG of SCC25NC and SCC25KD. (I) Detected changes in lipid sub-class. Levels of MG of SCC25NC and SCC25KD. (J) Detected changes in lipid sub-class. Levels of ChE of SCC25NC and SCC25KD. NS: no significance. NC: scrambled control shRNA, labeled with GFP for green fluorescence tracking; KD: shRNA targeting CAV2, labeled with GFP for green fluorescence tracking; CV: coefficient of variation; BPC: base peak intensity chromatogram; PCA: principal component analysis; OPLS-DA: orthogonal partial least square discriminant analysis; TG: triglyceride; MG: monoglycerol; ChE: cholesterol.

Supplementary Material 8: Table S5

Supplementary Material 9: Table S6

Supplementary Material 10: Table S7

Supplementary Material 11: S6. Integrated transcriptomic and lipidomic analysis of SCC25NC and SCC25KD. (A) Volcano plot for gene difference analysis. The abscissa is the fold change of the log2 transformation, and the ordinate is the ***P*** value of the -log10 transformation. Blue represented significantly down-regulated genes, red represented significantly upregulated genes, and insignificant genes were in gray. (B) Volcano map for lipid difference analysis. The abscissa is the fold change of the log2 transformation, and the ordinate is the ***P*** value of the -log10 transformation. Blue represented significantly down-regulated lipids, red represented significantly upregulated lipids, circles represented lipids with VIP greater than or equal to 1, and insignificant lipids were gray. (C-E) Gene and lipid PCA plot ((C) is the lipid PCA plot, (D) is the gene PCA plot, and (E) is the gene + lipid PCA plot). (F) The correlation coefficient of the small circle in the inner circle is 0.5, and that of the large circle in the outer circle is 1. With the circle point as the center, the chord formed by the two points has a positive correlation if the angle is less than 90; it is a negative correlation if it is greater than 90; the angle is 0; then the lipid is unrelated to the gene. Purple dots represented genes, and red squares represented lipids. Starting from the circle's center, the longer the line length is, the stronger the relationship is, and vice versa. Therefore, the correlation is generally strong, far from the center of the variable. (G) Circo's map of the correlation between differential genes and differential lipids. The line in the circle represented a correlation coefficient greater than or equal to 0.9 between the differential gene and the differential lipid. Peripheral blue and orange curves represented differential lipids and differential gene expression in both sets of samples. SCC25NC: SCC25 cells transfected with scramble shRNA; SCC25KD: SCC25 cells transfected with ***CAV2*** shRNA; PCA: principal component analysis; VIP:variable importance in projection.

Supplementary Material 12: S7. Transcriptomic analysis highlights mitochondrial dysfunction in SCC25NC and SCC25KD. (A and B) The bubble chart of KEGG pathways displayed the decreased oxidative phosphorylation and citrate cycle with significance. (C) The GO Cellular component bubble chart displayed the importance of the decreased mitochondrial respiratory chain complex I and respiratory chain. SCC25NC: SCC25 cells transfected with scramble shRNA; SCC25KD: SCC25 cells transfected with ***CAV2*** shRNA; KEGG: Kyoto Encyclopedia of Genes and Genomes.

Supplementary Material 13: S8 Correlation analysis of ***CAV2*** with key genes in OSCC. (A-F) Correlation analysis of the ***CAV2*** between ***PLIN3***, ***PNPLA2***, ***LIPE***, ***BCL2***, ***CAS3***, and ***CAS9*** from TCGA data. Correlation analysis was performed using Spearman's correlation (A-F). ***CAV2***: ***Caveolin2***; ***PLIN3***: ***Perilipin3***; CAS3: ***Caspase3***; CAS9: ***Caspase9***; OSCC: oral squamous cell carcinoma; TCGA: The Cancer GenomeAtlas.

Supplementary Material 14: S9 Dysregulated transcriptional repression of CAV2 by PPARγ in OSCC. (A-E) ***PPARG*** expression in OSCC of different clinical T stage, clinical N stage, clinical M stage, age, and gender from TCGA. n=334, 331, 328, 342, 345. (F) String-DB was used to predict the interaction of CAV2 and PPARγ with NCOR1. The search was limited to experimental evidence only, gathered from protein-protein interaction databases, with a minimum interaction score of 0.4. (A-E) Data were overlaid by the median and IQR. Significance was determined by the Kruskal-Wallis test with Dunn's multiple comparison tests (A-B) and the Wilcoxon rank sum test (D-E). IQR: interquartile range; CAV2: Caveolin2; PPARγ: peroxisome proliferator-activated receptor gamma; OSCC: oral squamous cell carcinoma; TCGA: The Cancer Genome Atlas.

Supplementary Material 15: S10 (A) The molecular docking of PPARγ inverse agonist T0070907 to the complex's human PPARgamma ligand binding domain crystal structure. (B-E) A logistic model was used to fit the growth for each concentration of T0070907 (0, 1, 2, 5, 10, 25, 50, 100 μM) in SCC25 and CAL27 cells stably expressed KD or NC after culturing for 24 h, 48 h, and 72 h. KD: shRNA targeting CAV2, labeled with GFP for green fluorescence tracking; NC: scrambled control shRNA, labeled with GFP for green fluorescence tracking. PPARγ: peroxisome proliferator-activated receptor gamma.

Acknowledgements
We thank Pro. Li Huang and Pro.Yuan He from the Medical Research Center for Structural Biology School of Basic Medical Sciences of Wuhan University for assistance with TEM. We also thank for Pro. Jing Zhang from the Department of Oral Medicine of School and Hospital of Stomatology of Wuhan University for help with reviewing, and Dr. Xiao-yu Zheng and Xin Wang from Wuhan University for assistance with experiments. Finally, we sincerely thank Pro. Yan Wang, Dr. Cuiping Yang, and Dr. Yingqiu Wang (Institute of Hydrobiology, Chinese Academy of Sciences) for AGILENT Seahorse XF24 technical support.

Author contributions
Y. Bai: conceptualization, formal analysis, data curation, investigation, methodology, writing–original draft, writing–review, and M. Jiang: data curation and methodology, and X. Chen: conceptualization, funding acquisition, writing–review, and editing. G. Zhou: conceptualization, resources, supervision, funding acquisition, validation, investigation, project administration, writing–review and editing.

Funding
This work was supported by the National Natural Science Foundation of China (grant no.82101023) to XJ Chen and the National Natural Science Foundation of China (grant no.82270983 and 82470982) to G Zhou.

Data availability
All data generated for this study will be made available to the corresponding author upon reasonable request.

Declarations

Ethics approval and consent to participate
The data utilized in this study were obtained from the publicly available TCGA database. All patient data in TCGA is de-identified and anonymized. The database is publicly accessible, and the use of its data complies with the ethical guidelines and policies for public data use. The Ethics Committee of the Hospital of Stomatology at Wuhan University approved animal research. The Ethics approval number for the animal experiments is S07921030H.

Consent for publication
Not applicable.

Competing interests
The authors declare no competing interests.

Author details
[1]The State Key Laboratory of Oral & Maxillofacial Reconstruction and Regeneration, Key Laboratory of Oral Biomedicine Ministry of Education, Hubei Key Laboratory of Stomatology, School & Hospital of Stomatology, Wuhan University, Wuhan, China
[2]Department of Oral Medicine, School and Hospital of Stomatology, Wuhan University, Wuhan, China

Received: 12 October 2024 / Accepted: 17 April 2025
Published online: 14 May 2025

References

1. Chow LQM. Head and neck Cancer. N Engl J Med. 2020;382(1):60–72.
2. Bray F, Ferlay J, Soerjomataram I, Siegel RL, Torre LA, Jemal A. Global cancer statistics 2018: GLOBOCAN estimates of incidence and mortality worldwide for 36 cancers in 185 countries. Cancer J Clin. 2018;68(6):394–424.
3. Sur S, Nakanishi H, Steele R, Zhang D, Varvares MA, Ray RB. Long non-coding RNA ELDR enhances oral cancer growth by promoting ILF3-cyclin E1 signaling. EMBO Rep. 2020;21(12):e51042.
4. Olzmann JA, Carvalho P. Dynamics and functions of lipid droplets. Nat Rev Mol Cell Biol. 2019;20(3):137–55.
5. Bai YT, Wang X, He MJ, Xie JR, Chen XJ, Zhou G. The potential of lipid Droplet-associated genes as diagnostic and prognostic biomarkers in head and neck squamous cell carcinoma. Comb Chem High Throughput Screen. 2024;27(1):136–47.
6. Chen XJ, Bai YT, Xie JR, Zhou G. Lipid droplets' functional protein caveolin-2 is associated with lipid metabolism-related molecule FABP5 and EMT marker E-cadherin in oral epithelial dysplasia. J Clin Pathol. 2024;77(5):330–7.
7. Fujimoto T, Kogo H, Ishiguro K, Tauchi K, Nomura R. Caveolin-2 is targeted to lipid droplets, a new membrane domain in the cell. J Cell Biol. 2001;152(5):1079–85.
8. Yang X, Ma L, Wei R, Ye T, Zhou J, Wen M, et al. Twist1-induced miR-199a-3p promotes liver fibrosis by suppressing caveolin-2 and activating TGF-β pathway. Signal Transduct Target Ther. 2020;5(1):75.
9. Borlido J, Sakuma S, Raices M, Carrette F, Tinoco R, Bradley LM, et al. Nuclear pore complex-mediated modulation of TCR signaling is required for Naïve CD4(+) T cell homeostasis. Nat Immunol. 2018;19(6):594–605.
10. Shatseva T, Lee DY, Deng Z, Yang BB. MicroRNA miR-199a-3p regulates cell proliferation and survival by targeting caveolin-2. J Cell Sci. 2011;124(Pt 16):2826–36.
11. Schubert W, Sotgia F, Cohen AW, Capozza F, Bonuccelli G, Bruno C, et al. Caveolin-1(-/-)- and caveolin-2(-/-)-deficient mice both display numerous skeletal muscle abnormalities, with tubular aggregate formation. Am J Pathol. 2007;170(1):316–33.
12. Wang Y, Wang Y, Liu R, Wang C, Luo Y, Chen L, et al. CAV2 promotes the invasion and metastasis of head and neck squamous cell carcinomas by regulating S100 proteins. Cell Death Discov. 2022;8(1):386.
13. Jiao F, Han T, Yuan C, Liang Y, Cui J, Zhuo M, et al. Caveolin-2 is regulated by BRD4 and contributes to cell growth in pancreatic cancer. Cancer Cell Int. 2020;20:55.
14. Liu F, Shangli Z, Hu Z. CAV2 promotes the growth of renal cell carcinoma through the EGFR/PI3K/Akt pathway. Onco Targets Ther. 2018;11:6209–16.
15. Goldberg IJ, Reue K, Abumrad NA, Bickel PE, Cohen S, Fisher EA, et al. Deciphering the role of lipid droplets in cardiovascular disease: A report from the 2017 National heart, lung, and blood Institute workshop. Circulation. 2018;138(3):305–15.
16. Kaushik S, Cuervo AM. Degradation of lipid droplet-associated proteins by chaperone-mediated autophagy facilitates lipolysis. Nat Cell Biol. 2015;17(6):759–70.
17. Liu R, Lee JH, Li J, Yu R, Tan L, Xia Y, et al. Choline kinase alpha 2 acts as a protein kinase to promote lipolysis of lipid droplets. Mol Cell. 2021;81(13):2722–e359.
18. Font-Díaz J, Jiménez-Panizo A, Caelles C, Vivanco MD, Pérez P, Aranda A, et al. Nuclear receptors: lipid and hormone sensors with essential roles in the control of cancer development. Semin Cancer Biol. 2021;73:58–75.
19. Kopchick JJ, Berryman DE, Puri V, Lee KY, Jorgensen JOL. The effects of growth hormone on adipose tissue: old observations, new mechanisms. Nat Rev Endocrinol. 2020;16(3):135–46.
20. Dubey V, Mishra AK, Ghosh AR. Appraisal of the possible role of PPARγ upregulation by CLA of probiotic Pediococcus pentosaceus GS4 in Colon cancer mitigation. PPAR Res. 2023;2023:9458308.
21. Wei Z, Wang Y, Peng J, Li H, Gu J, Ji N, et al. CircRFWD3 promotes HNSCC metastasis by modulating miR-27a/b/PPARγ signaling. Cell Death Discov. 2022;8(1):285.
22. Ma XX, Meng XQ, Wang YL, Liu Y, Shi XR, Shao S, et al. Ncor1 deficiency promotes osteoclastogenesis and exacerbates periodontitis. J Dent Res. 2023;102(1):72–81.
23. Battaglia S, Maguire O, Thorne JL, Hornung LB, Doig CL, Liu S, et al. Elevated NCOR1 disrupts PPARalpha/gamma signaling in prostate cancer and forms a targetable epigenetic lesion. Carcinogenesis. 2010;31(9):1650–60.
24. Liang X, Briaux A, Becette V, Benoist C, Boulai A, Chemlali W, et al. Molecular profiling of hormone receptor-positive, HER2-negative breast cancers from patients treated with neoadjuvant endocrine therapy in the CARMINA 02 trial (UCBG-0609). J Hematol Oncol. 2018;11(1):124.
25. Sun D, Wang J, Han Y, Dong X, Ge J, Zheng R, et al. TISCH: a comprehensive web resource enabling interactive single-cell transcriptome visualization of tumor microenvironment. Nucleic Acids Res. 2021;49(D1):D1420–30.
26. Puram SV, Tirosh I, Parikh AS, Patel AP, Yizhak K, Gillespie S, et al. Single-Cell transcriptomic analysis of primary and metastatic tumor ecosystems in head and neck Cancer. Cell. 2017;171(7):1611–e2424.
27. Tan YQ, Wang F, Ma RJ, Zhang J, Zhou G. Interferon-γ activated T-cell IRGM-autophagy axis in oral lichen planus. Int Immunopharmacol. 2021;94:107478.
28. Chen Y, Liang W, Liu K, Shang Z. FOXD1 promotes EMT and cell stemness of oral squamous cell carcinoma by transcriptional activation of SNAI2. Cell Biosci. 2021;11(1):154.
29. Wang X, He MJ, Chen XJ, Bai YT, Zhou G. Glaucocalyxin A impairs tumor growth via amplification of the ATF4/CHOP/CHAC1 cascade in human oral squamous cell carcinoma. J Ethnopharmacol. 2022;290:115100.
30. Kim D, Langmead B, Salzberg SL. HISAT: a fast spliced aligner with low memory requirements. Nat Methods. 2015;12(4):357–60.
31. Langmead B, Salzberg SL. Fast gapped-read alignment with bowtie 2. Nat Methods. 2012;9(4):357–9.
32. Li B, Dewey CN. RSEM: accurate transcript quantification from RNA-Seq data with or without a reference genome. BMC Bioinformatics. 2011;12:323.
33. Love MI, Huber W, Anders S. Moderated Estimation of fold change and dispersion for RNA-seq data with DESeq2. Genome Biol. 2014;15(12):550.
34. Crump K, Crouch E, Zelterman D, Crump C, Haseman J. Correcting for multiple comparisons in statistical analysis of animal bioassay data. Toxicol Sci. 2020;177(2):523–4.
35. Tan Z, Xiao L, Tang M, Bai F, Li J, Li L, et al. Targeting CPT1A-mediated fatty acid oxidation sensitizes nasopharyngeal carcinoma to radiation therapy. Theranostics. 2018;8(9):2329–47.
36. Chauhan MZ, Valencia AK, Piqueras MC, Enriquez-Algeciras M, Bhattacharya SK. Optic nerve lipidomics reveal impaired glucosylsphingosine lipids pathway in Glaucoma. Invest Ophthalmol Vis Sci. 2019;60(5):1789–98.
37. Wen B, Mei Z, Zeng C, Liu S. MetaX: a flexible and comprehensive software for processing metabolomics data. BMC Bioinformatics. 2017;18(1):183.
38. Dunn WB, Broadhurst D, Begley P, Zelena E, Francis-McIntyre S, Anderson N, et al. Procedures for large-scale metabolic profiling of serum and plasma using gas chromatography and liquid chromatography coupled to mass spectrometry. Nat Protoc. 2011;6(7):1060–83.
39. Yu G, Wang LG, Han Y, He QY. ClusterProfiler: an R package for comparing biological themes among gene clusters. OMICS. 2012;16(5):284–7.
40. Rohart F, Gautier B, Singh A, KA LC, mixOmics. An R package for 'omics feature selection and multiple data integration. PLoS Comput Biol. 2017;13(11):e1005752.
41. González I, Cao KA, Davis MJ, Déjean S. Visualising associations between paired 'omics' data sets. BioData Min. 2012;5(1):19.
42. Fathzadeh M, Li J, Rao A, Cook N, Chennamsetty I, Seldin M, et al. FAM13A affects body fat distribution and adipocyte function. Nat Commun. 2020;11(1):1465.
43. Wigger L, Barovic M, Brunner AD, Marzetta F, Schöniger E, Mehl F, et al. Multi-omics profiling of living human pancreatic islet donors reveals heterogeneous beta cell trajectories towards type 2 diabetes. Nat Metab. 2021;3(7):1017–31.
44. Casals N, Zammit V, Herrero L, Fadó R, Rodríguez-Rodríguez R, Serra D. Carnitine palmitoyltransferase 1 C: from cognition to cancer. Prog Lipid Res. 2016;61:134–48.
45. Zhu Y, Tian J, Peng X, Wang X, Yang N, Ying P, et al. A genetic variant conferred high expression of CAV2 promotes pancreatic cancer progression and associates with poor prognosis. Eur J Cancer. 2021;151:94–105.
46. Yamasaki T, Seki N, Yoshino H, Itesako T, Hidaka H, Yamada Y, et al. MicroRNA-218 inhibits cell migration and invasion in renal cell carcinoma through targeting caveolin-2 involved in focal adhesion pathway. J Urol. 2013;190(3):1059–68.
47. Lahiri V, Hawkins WD, Klionsky DJ. Watch what you (Self-) eat: autophagic mechanisms that modulate metabolism. Cell Metab. 2019;29(4):803–26.
48. Fang EF, Scheibye-Knudsen M, Chua KF, Mattson MP, Croteau DL, Bohr VA. Nuclear DNA damage signalling to mitochondria in ageing. Nat Rev Mol Cell Biol. 2016;17(5):308–21.
49. Newton K, Strasser A, Kayagaki N, Dixit VM. Cell death. Cell. 2024;187(2):235–56.

50. Cooke M, Kazanietz MG. Overarching roles of Diacylglycerol signaling in cancer development and antitumor immunity. Sci Signal. 2022;15(729):eabo0264.
51. Kong J, Ji Y, Jeon YG, Han JS, Han KH, Lee JH, et al. Spatiotemporal contact between peroxisomes and lipid droplets regulates fasting-induced lipolysis via PEX5. Nat Commun. 2020;11(1):578.
52. Perakakis N, Triantafyllou GA, Fernández-Real JM, Huh JY, Park KH, Seufert J, et al. Physiology and role of Irisin in glucose homeostasis. Nat Rev Endocrinol. 2017;13(6):324–37.
53. Yang M, Liang C, Swaminathan K, Herrlinger S, Lai F, Shiekhattar R, et al. A C9ORF72/SMCR8-containing complex regulates ULK1 and plays a dual role in autophagy. Sci Adv. 2016;2(9):e1601167.
54. Hoy AJ, Nagarajan SR, Butler LM. Tumour fatty acid metabolism in the context of therapy resistance and obesity. Nat Rev Cancer. 2021;21(12):753–66.
55. Dierge E, Debock E, Guilbaud C, Corbet C, Mignolet E, Mignard L, et al. Peroxidation of n-3 and n-6 polyunsaturated fatty acids in the acidic tumor environment leads to ferroptosis-mediated anticancer effects. Cell Metab. 2021;33(8):1701–e155.
56. Parry SA, Rosqvist F, Mozes FE, Cornfield T, Hutchinson M, Piche ME, et al. Intrahepatic fat and postprandial glycemia increase after consumption of a diet enriched in saturated fat compared with free sugars. Diabetes Care. 2020;43(5):1134–41.
57. Luo W, Gangwal K, Sankar S, Boucher KM, Thomas D, Lessnick SL. GSTM4 is a microsatellite-containing EWS/FLI target involved in Ewing's sarcoma oncogenesis and therapeutic resistance. Oncogene. 2009;28(46):4126–32.
58. Schuster S, Johnson CD, Hennebelle M, Holtmann T, Taha AY, Kirpich IA, et al. Oxidized Linoleic acid metabolites induce liver mitochondrial dysfunction, apoptosis, and NLRP3 activation in mice. J Lipid Res. 2018;59(9):1597–609.
59. Palikaras K, Lionaki E, Tavernarakis N. Mechanisms of mitophagy in cellular homeostasis, physiology and pathology. Nat Cell Biol. 2018;20(9):1013–22.
60. Borsini A, Stangl D, Jeffries AR, Pariante CM, Thuret S. The role of omega-3 fatty acids in preventing glucocorticoid-induced reduction in human hippocampal neurogenesis and increase in apoptosis. Transl Psychiatry. 2020;10(1):219.
61. Montecillo-Aguado M, Tirado-Rodriguez B, Huerta-Yepez S. The involvement of polyunsaturated fatty acids in apoptosis mechanisms and their implications in Cancer. Int J Mol Sci. 2023;24(14).
62. Xia DN, Tan YQ, Yang JY, Zhou G. Omega-3 polyunsaturated fatty acids: a promising approach for the management of oral lichen planus. Inflamm Res. 2020;69(10):989–99.
63. Brunmeir R, Xu F. Functional regulation of PPARs through Post-Translational modifications. Int J Mol Sci. 2018;19(6).
64. Brust R, Shang J, Fuhrmann J, Mosure SA, Bass J, Cano A, et al. A structural mechanism for directing corepressor-selective inverse agonism of PPARγ. Nat Commun. 2018;9(1):4687.

Publisher's note